PARTICLE-IMAGING TECHNIQUES FOR EXPERIMENTAL FLUID MECHANICS

Ronald J. Adrian

Department of Theoretical and Applied Mechanics, University of Illinois, Urbana, Illinois 61801

INTRODUCTION

An important achievement of modern experimental fluid mechanics is the invention and development of techniques for the measurement of whole, instantaneous fields of scalars and vectors. These techniques include tomographic interferometry (Hesselink 1988) and planar laser-induced fluorescence for scalars (Hassa et al 1987), and nuclear-magnetic-resonance imaging (Lee et al 1987), planar laser-induced fluorescence, laser-speckle velocimetry, particle-tracking velocimetry, molecular-tracking velocimetry (Miles et al 1989), and particle-image velocimetry for velocity fields. Reviews of these methods can be found in articles by Lauterborn & Vogel (1984), Adrian (1986a), Hesselink (1988), and Dudderar et al (1988), and in books written by Merzkirch (1987) and edited by Chiang & Reid (1988) and Gad-el-Hak (1989).

Pulsed-Light Velocimetry

The subject of the present article, particle-imaging techniques, is a member of a broader class of velocity-measuring techniques that measure the motion of small, marked regions of a fluid by observing the locations of the images of the markers at two or more times. These methods return to

261

the fundamental definition of velocity and estimate the local velocity **u** from

$$\mathbf{u}(\mathbf{x}, t) \doteq \frac{\Delta \mathbf{x}(\mathbf{x}, t)}{\Delta t}, \tag{1}$$

where $\Delta \mathbf{x}$ is the displacement of a marker, located at **x** at time t, over a short time interval Δt separating observations of the marker images. The particles are usually solids in gases or liquids but can also be gaseous bubbles in liquids or liquid droplets in gases or immiscible liquids. Other types of markers include (*a*) patches of molecules that are activated by laser beams, causing them either to fluoresce (Gharib et al 1985), or to change their optical density by photochromic chemical reactions (Popovich & Hummel 1967, Ricka 1987), and (*b*) speckle patterns caused by illuminating *groups* of particles with coherent light. Regardless of the marker type, locations at various instants are recorded optically by pulses of light that freeze the marker images on an optical recording medium such as a photographic film, a video array detector, or a holographic film. Since these methods share many similarities, it is useful to group them under the single topic of *pulsed-light velocimetry*, or *PLV*.

The various PLV techniques are organized in Figure 1.

Particle-Image Velocimetry

A technique that uses particles and their images falls into the category commonly known as *particle-image velocimetry*, or *PIV*, which is the principal subject of this article. Before comparing the characteristics of PIV with the other methods displayed in Figure 1, it is helpful to examine
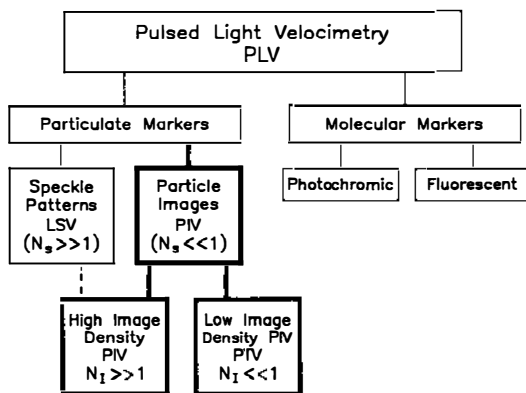
Figure 1   Particle-image velocimetry and other forms of pulsed-light velocimetry.

a typical PIV system in somewhat greater detail. To this end, a planar particle-image velocimeter optical system is shown in Figure 2. Particles in the fluid are illuminated by a sheet of light that is pulsed. The particles scatter light into a photographic lens located at 90° to the sheet, so that its in-focus object plane coincides with the illuminated slice of fluid. Images are formed on a photographic film or on a video array detector, and the images are subsequently transferred to a computer for automatic analysis. The analysis of the recorded image field is one of the most important steps in the entire process, as it couples with the image-acquisition process to determine the accuracy, reliability, and spatial resolution of the measurements; it is also the most time-consuming part of the process. Image analysis, or "interrogation," is discussed in detail later. If the recorded image field contains a small amount of information, as for a typical video camera that consists of an array of approximately 500×500 pixels, the entire image field (e.g. 2.5×10^5 pixels) can be digitized and passed to the computer in one file. If the image field is very rich in information, as for a 100 mm $\times$ 125 mm piece of 300 lines mm^{-1} resolution photographic film containing over 1.1×10^9 pixels, the local velocity in a small region of the image field is found by digitizing an *interrogation spot* and analyzing the images within the spots, one spot at a time. The vector field is obtained by repeating this process on a grid of such interrogation spots.

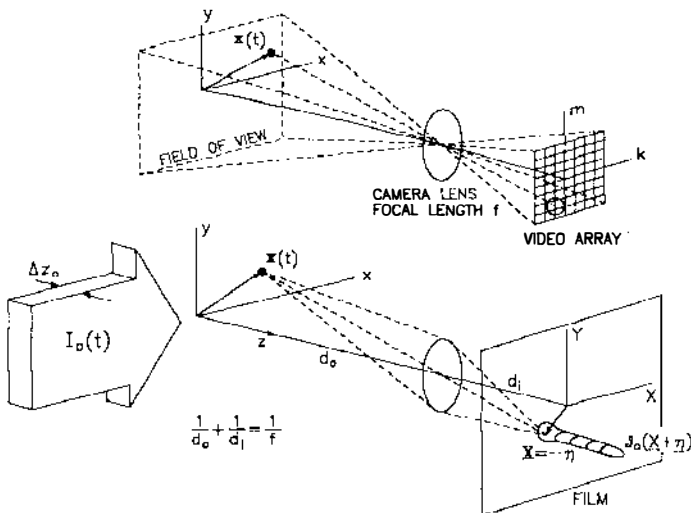An example of a small portion of a vector field measured by the latter

Figure 2 Optical system of a planar particle-image velocimeter. (*Top*) Video recording; (*bottom*) photographic recording.

techni**q**ue is shown in Figure 3. Each vector was obtained from a 1 mm × 1 mm interrogation spot, and the spacing of the spots is also 1 mm (Landreth & Adrian 1990).

Modes of Operation

Broadly speaking, the system and procedures just described for PIV are similar for each of the particle-marker techniques shown in Figure 1, and it is convenient in many ways to view them as three different modes of operation of the same instrument. The differences between particle-image velocimetry and laser-speckle velocimetry have to do with the effects of the mean number concentration of scattering particles per unit volume, C, upon the image field and in relation to the scales of the fluid flow field.

LASER-SPECKLE MODE   In the laser-speckle mode, the concentration of scattering particles in the fluid is so large that the images of the particles overlap in the image plane. The random phase differences between the images of individual randomly located particles create the random interference patterns commonly known as laser speckle (Dainty 1975). The
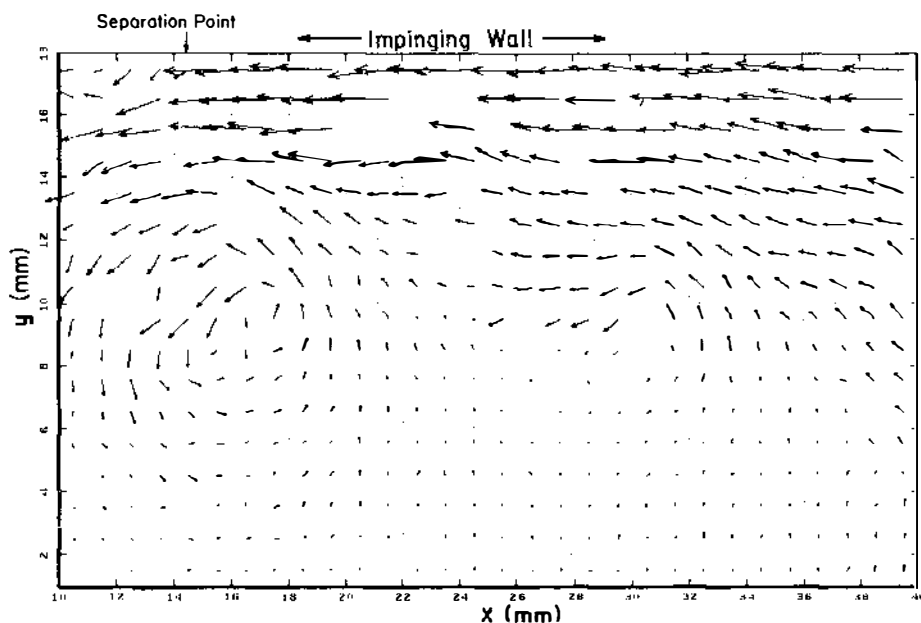
Figure 3 Small section of the vector field of an impinging wall jet measured by PIV (reproduced with permission from Landreth & Adrian 1990).

local speckle pattern is the superposition of images from a local group of scattering particles, and as such it translates with the group of particles. Hence, velocity can be measured by measuring speckle displacement, and operation in this mode is called *laser speckle velocimetry*, or *LSV*.

PARTICLE-TRACKING MODE   In the particle-image mode the concentration of scatterers is low enough to render overlapping images improbable, and individual particle images dominate. Within this regime of concentrations, two limits exist. In the low-image-density limit the concentration of scatterers is so small that images are sparse in the image plane. Multiple exposures or streak exposures of individual particles leave tracks that are short compared with the mean spacing between particles, so that individual images are easily identified. Since the number of images per unit area is small, it is feasible to measure displacements by tracking individual images. Hence, the low-image-density mode of PIV is often referred to as *particle-tracking velocimetry*, or *PTV*.

HIGH-IMAGE-DENSITY PIV MODE   The high-image-density mode of PIV occurs when concentrations lie between those of LSV and PTV. The concentrations are high enough to guarantee that every interrogation spot in the image field contains many images, but not so high that the images overlap to produce speckle. In this mode, the abundance of images makes tracking individual particles time consuming, and one measures instead the displacements of small groups of images.

Historical Development

Although it is useful to view high-image-density PIV and PTV as limiting extremes of the general class of particle-imaging techniques in order to unify that part of the theory and practice that is common to each, this unification does not reflect the historical development of these techniques. Many of the approaches used in PTV are natural extensions of classical flow-visualization techniques, whereas many elements of low-image-density PIV and especially high-image-density PIV grew out of laser-speckle velocimetry.

Particle-tracking velocimetry has its roots in flow-visualization techniques such as particle-streak photography and stroboscopic photography, of which several beautiful examples can be found in Van Dyke (1982). Because of the simplicity of the particle-tracking concept, quantitative (or at least semiquantitative) results have been available from this technique for decades, provided one was willing to perform manual analysis (cf Fage & Townend 1932). The thrusts of modern developments in PTV have been to make the technique more quantitative and to computerize the analysis of images.

Laser-speckle velocimetry has its roots in solid mechanics, where coherent light scattered from solid surfaces naturally forms speckle patterns (Erf 1980, Archbold & Ennos 1972). Unlike PTV, simple manual analysis of a double-exposed specklegram is not feasible, because the human eye cannot untangle the superposed speckle fields. Analysis of such fields became possible with the development of the Young's fringe method of interrogation (Burch & Tokarski 1968, Stetson 1975) in which an interrogation spot on a double-exposed specklegram is illuminated by a laser beam. The speckle field from each exposure diffracts a light wave from the coherent interrogation beam, which interferes with the other wave to form a Young's fringe pattern (Figure 4). The orientation of the fringes is perpendicular to the direction of the displacement, and the spacing is inversely proportional to the magnitude of the displacement. This technique addressed the issue of comparing the speckle field from the first
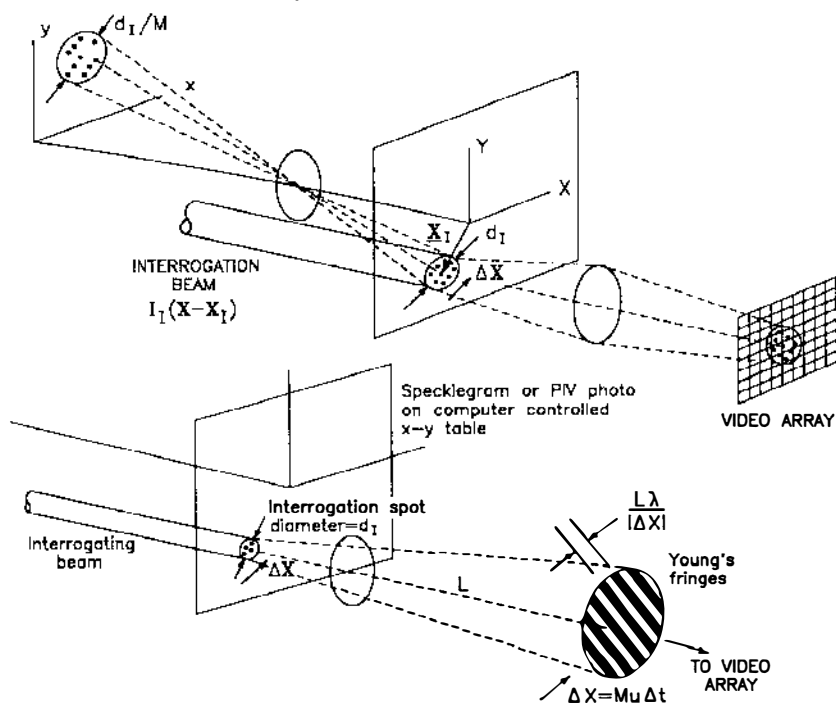

Figure 4 Interrogation of a photograph. (*Top*) Direct-image digitization; (*bottom*) Young's fringe method in which a lens performs on an optical two-dimensional Fourier transform of the image field in the interrogation spot.

exposure with the field from the second exposure and statistically pairing them speckle by speckle.

Early experiments by Dudderar & Simpkins (1977), Grousson & Mallick (1977), and Barker & Fourney (1977) showed that the laser-speckle technique could be applied to measure fluid motion in simple, steady laminar flows using the Young's fringe method of interrogation. Simpkins & Dudderar (1978) and Meynart (1980, 1983a,b,c, 1985) pioneered much of the development of LSV and its application to more complex flows, including a turbulent jet and thermal convection.

High-image-density particle-image velocimetry was established as a distinct mode of pulsed-light velocimetry by Pickering & Halliwell (1984) and Adrian (1984), who argued that the concentrations of scattering particles that are practical in experimental fluid mechanics are often not dense enough to create speckle patterns. Thus, unless one makes extreme efforts to seed the flow with high concentrations of carefully chosen particles, high-image-density PIV is more likely than LSV. Many experiments that had been labeled LSV were indeed PIV, as Meynart (1983a) seems to have recognized. Further studies of the scattering properties of particles in relation to photographic imaging (Adrian & Yao 1985) indicated that individual particles in the 1–10 μm range would produce more detectable images at lower mass loadings than the large numbers of fine particles that would be needed to produce speckle. This result is much like the finding in laser-Doppler velocimetry that it is better to use incoherent detection than coherent detection in most cases (Drain 1972).

Although high-image-density PIV resembles LSV in many regards, this article focuses on the particle-image mode, with the *proviso* that many of the concepts and developments will be applicable to LSV as well. Topics that are common to particle imaging in general are discussed first, followed by separate sections for the high- and low-image-density cases.

PARTICLES AND THEIR IMAGES

Single-Particle Imaging

Given an ideal, aberration-free lens of focal length f, the image of a small particle at $\mathbf{x}$ in the fluid is mapped onto the point $-\boldsymbol{\eta}$ in the image plane of the lens, where

$$\boldsymbol{\eta} = \frac{d_i}{d_o - z}[x\hat{\mathbf{x}} + y\hat{\mathbf{y}}]. \tag{2}$$

Here d_o and d_i are the object and image distances, respectively, $\hat{\mathbf{x}}$ and $\hat{\mathbf{y}}$ are unit vectors perpendicular to the optic axis of the lens, and z is the distance

away from the object plane. The magnification depends upon z according to

$$M(z) = \frac{d_i}{d_o - z},$$ (3)

and this dependence embodies the usual rules of perspective. In particular, it is noted that erecting the image takes $-\boldsymbol{\eta}$ into $\boldsymbol{\eta}$, so that a small displacement of a particle in the fluid results in an erected-image displacement given by

$$\Delta \mathbf{X} = M(0)\,(\Delta x \hat{\mathbf{x}} + \Delta y \hat{\mathbf{y}}) + M(0)\frac{(x\hat{\mathbf{x}} + y\hat{\mathbf{y}})}{d_o}\Delta z.$$ (4)

These equations refer to coordinates centered on the camera axis and ideal lenses. Generalized equations for arbitrary coordinates and lenses with aberrations are presented by Murai et al (1980).

The intensity of the image in the nominal image plane at d_i, per unit of illuminated beam intensity $I_o(t)$, is denoted by $\mathscr{I}_o(\mathbf{X} + \boldsymbol{\eta}(\mathbf{x}); \mathbf{x})$. The diameter of the image is determined by the diameter of the particle d_p, the magnification, and the point response function of the lens. If the lens is diffraction limited, the point response function is an Airy function of diameter

$$d_s = 2.44(1+M)f^{\#}\lambda,$$ (5)

where $f^{\#}$ is the f-number of the lens, and λ is the wavelength of light. The image of a finite-diameter particle is the convolution of the Airy function with the geometric image of the particle (Goodman 1968). Approximating both functions by Gaussians leads to the following approximate formula for the image diameter (Adrian & Yao 1985):

$$d_e = (M^2 d_p^2 + d_s^2)^{1/2}.$$ (6)

For typical values of the parameters (say $M = 1$, $f^{\#} = 8$, and $\lambda = 0.6993$ μm), $d_s = 25$ μm, so d_e is approximately independent of the particle size for particle diameters less than about 10 μm. Conversely, for particle diameters greater than 50 μm, the image diameter is essentially Md_p.

The foregoing equations pertain when the particle is within the depth of field of the lens, given by

$$\delta z = 4(1+M^{-1})^2 f^{\#2}\lambda.^1$$ (7)

Outside of this range the image is blurred by an amount exceeding 20%

---

[1] This formula, due to P. W. Offutt, generalizes the conventional result to values of M not equal to unity.

of the in-focus diameter. The parametric dependence of $\mathscr{I}_0$ upon $\mathbf{x}$ is needed to represent out-of-focus effects. Within the depth of focus, $\mathscr{I}_0$ depends on $\mathbf{x}$ only through $\boldsymbol{\eta}$.

The depth-of-field places a strong constraint on an imaging system. For example, the depth of field for $f^\# = 8$ and $\lambda = 0.6993$ μm is only 0.7 mm. Hence, if one seeks to image small particles with high spatial resolution, the depth of field is inherently small, and it is appropriate to use a thin light sheet to illuminate just that region over which the particles are in-focus. Typically, that region is of order 1 mm. Conversely, if one seeks to image over a deep region, as in three-dimensional particle tracking, then the requirement for large depth of focus implies that the f-number, and hence the image diameters, must be large. For example, for an 11-mm depth of field, $f^\#$ must be increased by a factor of four, and the value of d_s exceeds 100 μm.

The field of view of the camera depends upon the maximum angular range over which the lens operates and the size of the film or the detector array as projected back into the fluid. The field of view defines a maximum value for the in-plane location of the particle, $|\mathbf{x}|_{\max}$. If $|\mathbf{x}|_{\max}/d_0$ is small, the second term in Equation (4) is correspondingly small, and the two-dimensional displacement of the erected image is related to the in-plane displacement of the particle by $\Delta\mathbf{X} = M(0)\Delta\mathbf{x}$. [Here and elsewhere, $\Delta\mathbf{x} = (\Delta x, \Delta y)$ will be understood to be a two-dimensional vector when its appearance in an equation with $\Delta\mathbf{X}$ demands two-dimensionality for consistency.] We refer to this situation as "paraxial photography." Again, for example, if $f = 300$ mm and the field of view is 120 mm at $M = 1$, $|\mathbf{x}|_{\max}/d_0$ will be less than 0.1.

If the paraxial approximation is not satisfied, measurements of the in-plane displacements Δx and Δy are contaminated by the out-of-plane displacement Δz (Lourenco & Whiffen 1986). The obvious remedy for this situation is stereoscopic photography. Consider two identical lenses separated by $2d_L$ and imaging onto separate photographs (Figure 5). The equations for each lens are
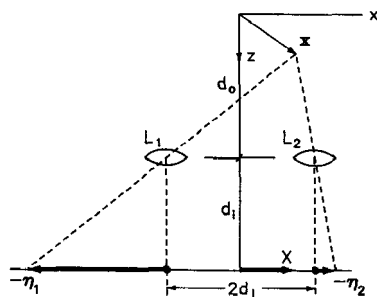

Figure 5 Stereographic imaging to resolve the three-dimensional vector field on a planar domain.

$$\boldsymbol{\eta}_1 = \frac{d_i}{d_o - z}[(x + d_L)\hat{\mathbf{x}} + y\hat{\mathbf{y}}], \tag{8a}$$

$$\boldsymbol{\eta}_2 = \frac{d_i}{d_o - z}[(x - d_L)\hat{\mathbf{x}} + y\hat{\mathbf{y}}], \tag{8b}$$

from which it is clear that measurements of the displacements of the left
and right images can be used to solve for Δx, Δy, and Δz. The method
provides accurate measurements of the in-plane displacements and some-
what less accurate estimates of the out-of-plane component (Sinha 1988).

Distribution of Particles and Images

POISSON DISTRIBUTION   The mean number of particles per unit volume, C,
determines the maximum number of potential sites at which velocities can
be measured, as well as the mode of operation of the PIV. If the particles
arc modclcd as randomly distributed points, the probability of finding k
particles in a volume V obeys a Poisson distribution, i.e.

$$\text{Prob}(k \text{ particles in } V) = \frac{(CV)^k}{k!}e^{-CV}. \tag{9}$$

SOURCE DENSITY   The source density, referrcd to carlicr, is dcfincd as the
mean number of particles in a cylindrical volume formed by the intersection
of the illuminating light sheet with a circle whose diameter d_e/M is that of
the particle image projected back into the fluid (Adrian 1984). This volume
is called a *resolution cell*. The value of the source density is

$$N_s = C\Delta z_o \frac{\pi d_e^2}{4M^2}. \tag{10}$$

If two particles lay within a resolution cell, their images must overlap in the
image plane. From Equation (9) the probability of two or more particles in
this volume becomes significant as N_s exceeds unity. Hence, large N_s implies
the formation of speckle patterns in the image plane. Conversely, small N_s
implies a low probability of more than one particle in a resolution cell,
since $\text{Prob}(k) \sim N_s^k/k!$ for small N_s. Hence, small N_s implies solitary images,
e.g. the particle-image limit.

IMAGE DENSITY   Similar reasoning can be applied to the number of particle
images within an *interrogation cell*, defined as the intersection of the light
sheet with a circle whose diameter d_i/M is equal to the diameter of an
interrogation spot projected back into the fluid. (If an interrogation spot
is not used, d_i/M can be replaced by the maximum two-dimensional
displacement of the particles, $|\Delta \mathbf{x}|_{max}$.) The interrogation spot on the image

plane will contain more than one image if there is more than one particle in the volume $\Delta z_o \pi d_1^2 / 4M^2$. Thus, an appropriate image-density parameter is defined to be (Adrian & Yao 1984)

$$N_1 = C\Delta z_o \pi d_1^2 / 4M^2. \tag{11}$$

If $N_1 \ll 1$, the probability of finding more than one particle in an interrogation cell is small compared with the probability of finding one particle in the cell, corresponding to the low-image-density limit. If $N_1 \gg 1$, there will almost always be many images in the interrogation spot. That is, the probability of any interrogation spot failing to contain particles is small.

PARTICLE SAMPLING OF THE VELOCITY FIELD   The PIV technique effectively samples the velocity of the fluid at the random location of each particle. The frequency with which this sampling occurs can be characterized by the mean distance between nearest neighboring particles in the fluid volume (given by $\bar{r} = 0.55C^{-1/3}$) or by the mean distance between nearest neighboring images in the planar projection of the light sheet, [given by $0.5(C\Delta z_o)^{-1/2}$]. If the particles were regularly located on a three-dimensional periodic grid, the entire velocity field could be perfectly reconstructed from the velocity samples, provided that Nyquist's criterion, which requires that the sample spacing be less than one half of the smallest wavelength in the field, was satisfied. Since the particle spacing is not regular, the Nyquist sampling theorem does not apply in the usual sense, but results concerning random sampling of one-dimensional processes indicate that reconstruction will be *inaccurate* for scales smaller than several times the mean data spacing (Adrian & Yao 1987).

The data spacing is only relevant in relation to the length scales of the flow field. For turbulence the integral length scale, characteristic of the energy-containing motions, could be one such scale. Sampling at a mean rate smaller than the integral scale and interpolating to obtain a smooth field reveals the energy-containing motions, albeit in a form that is both smoothed by the interpolation process and randomized by the small-scale component of the velocity at each sample point.

To differentiate turbulent data with accuracy, the mean spacing between samples should be much less than the Taylor microscale λ_T, since λ_T represents the length scale of the velocity gradients. Generalizing a concept from laser-Doppler velocimetry (Adrian 1983), it is useful to define the *data density* as

$$N_\lambda \equiv C\lambda_T^3. \tag{12}$$

In terms of this density, the mean spacing between samples relative to the Taylor microscale is

$$\bar{r}/\lambda_T = 0.55/N_\lambda^{1/3}. \tag{13}$$

Thus, large values of N_λ imply high sampling rates relative to λ_T. In this limit the data can be differentiated accurately, and, in particular, vorticity and rate of strain may be computed. Although any smooth field obtained by interpolation over randomly sampled data can be differentiated, the results will be inaccurate unless $N_\lambda \gg 1$. Quantitative limits on this inequality need to be determined.

Experimentally, the spatial resolution of a PIV is determined by Δz_o (or δz if $\delta z < \Delta z_o$) and by the diameter of the interrogation spot d_I/M (or the maximum two-dimensional displacement $|\Delta x|_{max}$ if an interrogation spot is not used). Let us assume that $|\Delta x|_{max} < d_I/M$ and $\delta z > \Delta z_o$, so that the spatial resolution is defined by the resolution cell. Then, the ratio of data density to image density is $N_\lambda = [4M^2\lambda_T^3/\pi\Delta z_o d_I^2]N_I$, and if Δz_o and d_I are of order λ_T or smaller, we see that a high image density implies a high data density. Thus, the high-image-density limit maximizes the spatial resolution of the PIV.

LIGHT SCATTERING   The flux of light energy scattered from an illuminating beam of intensity I_o by a particle into a cone of solid angle Ω is given by

$$I_o \int_\Omega \frac{\lambda^2 \sigma \cdot \sigma^*}{4\pi^2} d\Omega,$$

where σ is the Mie scattering coefficient of the particle (Kerker 1969). The scattered light energy as a function of the particle diameter oscillates erratically about a generally increasing mean value (Figure 6). The average energy increases as $(d_p/\lambda)^4$ in the Rayleigh scattering range $(d_p \ll \lambda)$, and as $(d_p/\lambda)^2$ in the geometric scattering range $(d_p \gg \lambda)$.

The ratio of the refractive index of the particle to that of the fluid is a significant parameter in light scattering. Because the refractive index of water is 1.33 times that of air, particles in air scatter at least ten times more effectively than particles in water. Hence, experiments in water and other liquids require larger particles, or larger illumination. Fortunately, larger particles can be used in liquid flows without loss of tracking fidelity.

Mie scattering calculations for the light energy collected by a camera lens in side-scatter have been performed for small (1–20 μm) particles in air and water (Adrian & Yao 1985). The results can be used to estimate the strength of a particle image for various particle sizes, f-numbers, light-sheet geometries, light-source pulse energies, and film or detector sensitivities.
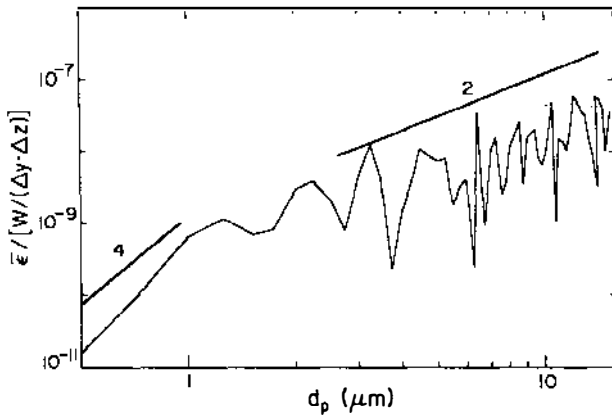
Figure 6 Mean exposure per unit illuminating intensity for light side-scattered into an $f \# 22$ lens. The ratio of the particle refractive index to the fluid refractive index is 1.2. The *solid lines* indicate square-law and four-power slopes (reproduced with permission from Adrian & Yao 1985).

The optical density of an image recorded on film or the electrical output produced by an image striking a photo detector array are each proportional to the optical exposure $\varepsilon(\mathbf{X})$, defined as the energy per unit area, $\mathscr{I}\delta t$. The mean exposure averaged over the area of a particle image is given by

$$\bar{\varepsilon} = \frac{\lambda^2 W \int |\sigma|^2 \, d\Omega}{\pi^3 (M^2 \overline{d_p^2} + 2.44^2 (1 + M)^2 f^{\#\,2} \lambda^2) \overline{\Delta y_0} \overline{\Delta z_0}}, \tag{14a}$$

$$\sim \frac{\lambda^2 W d_p^n D_e^2}{\lambda^n d_0^2 (M^2 \overline{d_p^2} + 2.44^2 d_i^2 \lambda^2 / D_a^2) \overline{\Delta y_0} \overline{\Delta z_0}}, \tag{14b}$$

where W is the energy of the light pulse, D_a is the lens aperture diameter $(f^\# = f/D_a)$, and n is the power-law exponent describing the scattered light energy. For recording on Kodak Technical Pan film, a relatively insensitive but good-resolution film, calculations indicate that particles as small as 1–2 μm can be photographed in air using 2.5-J ruby-laser pulses. Experience indicates that particles of the same size can be photographed in air flows using lower powered Nd: Yag lasers (Kompenhans & Höcker 1988). The same energy permits particles of order 10 μm to be photo-

graphed in water. More sensitive film or metallic coatings on the particles permit smaller particles (e.g. see Paone et al 1989).

Equations (14a) and (14b) contain several simple, but important, implications. For small particles in the 1–10 μm range, n is of order three, and diffraction blurring dominates the denominator, so that

$$\bar{\varepsilon} \sim W d_{\mathrm{p}}^3 D_{\mathrm{a}}^4 / d_{\mathrm{o}}^2 d_{\mathrm{i}}^2 \lambda^3 \Delta y_{\mathrm{o}} \Delta z_{\mathrm{o}}. \tag{15}$$

One sees that the intensity drops rapidly with increased size of the system. Specifically, if d_{o}, d_{i}, and Δy_{o} are each scaled up by a factor of m, the intensity of an image decreases by m^{-5}. The intensity also varies as λ^{-3} owing to the combined effects of Mie scattering and diffraction spreading of the image into a spot, whose area is proportional to λ^2. It is also found that many films are significantly more sensitive to shorter wavelengths, and that the minimum thickness of the light sheet is $\Delta z_{\mathrm{o}} \sim \lambda$. Hence, all of these effects combine to make short wavelengths (e.g. green light) much more effective than long wavelength (e.g. red light).

The cubic dependence on particle diameter should also be noted, as it implies that the image field will be biased heavily toward larger particles that may or may not follow the flow. In this regard, it is desirable to use uniform particles.

As the particle size increases into the geometric scattering regime, Equation (15) becomes

$$\bar{\varepsilon} \propto \frac{W D_{\mathrm{a}}^2}{d_{\mathrm{o}}^2 M^2 \Delta y_{\mathrm{o}} \Delta z_{\mathrm{o}}}, \tag{16}$$

which implies (perhaps surprisingly) that the image intensity becomes independent of the particle diameter, because both the scattered light energy and the image area increase as d_{p}^2. Thus, beyond a certain size, of order 100 μm, there is little to be gained by using bigger particles.

PARTICLE DYNAMICS   All PIV methods inherently measure the Lagrangian velocities of particles, $\mathbf{v}$. If the particle velocity is being used to infer Eulerian fluid velocity $\mathbf{u}(\mathbf{x}, t)$, one must consider the accuracy with which a particle follows the fluid motion. With subscript "p" denoting particulate properties, the equation of motion of a single particle in a dilute suspension (e.g. noninteracting particles) is

$$\rho_{\mathrm{p}} \frac{\pi d_{\mathrm{p}}^3}{6} \frac{d\mathbf{v}}{dt} = C_{\mathrm{D}} \frac{\rho \pi d_{\mathrm{p}}^2}{4} |\mathbf{v} - \mathbf{u}| (\mathbf{v} - \mathbf{u}) \tag{17}$$

plus corrections for the added mass of the fluid, unsteady drag forces, pressure gradients in the fluid, and nonuniform fluid motion. In gaseous flows with relatively heavy solid or liquid particles, we may ignore all terms

except the static drag law with drag coefficient C_D. This term incorporates finite-Reynolds-number effects.

Particle response is often described in terms of the flow velocity and some frequency of oscillation, and the first question is, how fast can the flow be before the particle lag $|\mathbf{v}-\mathbf{u}|$ creates an unacceptably large error? An appropriate approach is to evaluate the particle slip velocity as a function of the applied acceleration. For the simplified drag law of Equation (17), one has

$$|\mathbf{v}-\mathbf{u}| = \left[\frac{2}{3}\frac{\rho_p}{\rho}\frac{d_p}{C_D}\right]^{1/2} \tag{18}$$

showing that the slip velocity for finite particle Reynolds number, where $C_D \sim$ constant, is only proportional to the square root of the acceleration.

In the limit of small particle Reynolds number $|\mathbf{v}-\mathbf{u}|d_p/v \ll 1$, Stokes' law may be used to evaluate C_D, resulting in

$$|\mathbf{v}-\mathbf{u}| = \rho_p d_p^2 |\dot{\mathbf{v}}|/36\rho v. \tag{19}$$

Some exemplary calculations are illuminating. Consider an airflow with velocity differences of 100 m s^{-1} occurring over a 0.01-m length scale. The acceleration is of the order of 10^6 m s$^{-2} = 100,000g$, where g is the gravitational constant. The slip velocity of a 1-μm particle of specific gravity 2 is about 4 m s^{-1}, or 4% of the velocity change. In support of these estimates, laser-Doppler velocimeter measurements in a 499 m s^{-1}/92 m s^{-1} planar shear layer in air with a thickness ranging from 6 to 15 mm indicate that 0.5-μm polystyrene latex particles are able to follow the turbulent eddies in the shear layer with accuracy better than 5% of the difference across the shear layer (Goebel & Dutton 1990).

Illumination and Recording

PULSE CODES   Various pulse codes are illustrated in Figure 7, wherein the illuminating intensity I_o is shown as a function of time, and the image patterns resulting from a single particle are shown in the frames. In the case of *single-frame recording* the images from several pulses are superimposed on a record that may consist of one frame of film or one electronic frame from a video-camera output. In either case, the total exposure of the frame is the integral of the exposures during the frame opening time, and once a frame is exposed the total exposure cannot be separated into its component exposures. *Multiframing* refers to cinematic film or sequences of video-image frames.

The primary function of the pulse code is to provide images at two precisely determined times, separated by Δt, from which $\Delta \mathbf{x}$ can be
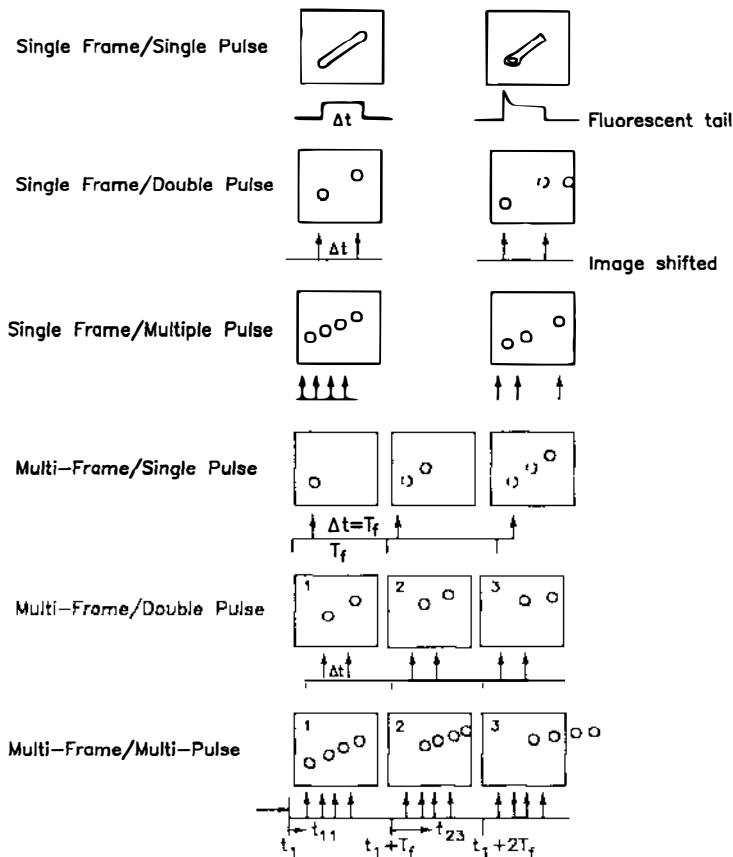
Figure 7 Pulse-coding and framing methods.

measured. A secondary function is to provide additional information that makes image analysis easier. The purpose of multiframing can be either to provide a sequential time history of the velocity or to make image analysis easier.

The time separation Δt is the single most important adjustable variable in a PIV system, as it determines the maximum and minimum velocities that can be measured. The *duration* of the light pulses, δt, determines the degree to which an image is frozen during the pulse exposure. Steady light sources such as ordinary lamps or CW lasers can be chopped or modulated to form the pulses, but this often wastes considerable energy, in that the fraction of energy utilized is proportional to $\delta t/\Delta t$, and this number should

be small to avoid blurring of the image. It is more efficient to use pulsed sources such as flash lamps, spark discharges, or pulsed lasers.

Xenon flash lamps can emit several hundred joules in pulses as short as 1 μs, but only a small fraction of this energy can be used to form a thin, high-quality light sheet owing to inherent limits on collimating light from an extended source. Spark discharges are narrower.

Pulsed lasers emit energy in collimated beams that can be formed efficiently into light sheets. Pulsed metal-vapor lasers produce green 10-ns pulses repetitively at free-running frequencies in the 5–20 kHz range and energies of order 10 mJ. These lasers are suitable for in-line holograms or for photographing large particles in side-scatter. The time between pulses can be lengthened by replacing the free-running frequency with an appropriate pulse sequence for a brief interval, but very short time delays (e.g. less than 10 μs) are not readily available.

Pulsed ruby lasers produce 3–5 ms long fluorescence pulses of 699.3-nm light that can be Q-switched two to four times during the fluorescence lifetime to produce sharp, 25-ns-long pulses with energies of order 1–10 J. The pulses can be separated by Δt's as small as 1 μs and as large as about 1 ms. To achieve time delays from a few milliseconds to several seconds in a double-pulsed mode, the laser rod can be pumped twice and Q-switched each time. Unfortunately, the time to recharge the capacitor banks is long, so that ruby lasers typically do not fire a double pulse more often than once per minute.

Frequency doubled-pulsed Nd : Yag lasers fire 10-ns pulses at 532-nm light repetitively at rates up to 50 Hz, and two lasers can be combined to produce periodic trains of double pulses suitable for multiframing at 10–50 Hz with virtually any separation between the double pulses. These systems are perhaps the most versatile of all of the available light sources. The lower pulse energy of the Nd : Yag laser relative to the ruby laser is largely compensated by the shorter wavelength, which leads to improved scattering, thinner light sheets, and smaller images [cf Equation (14b)].

The energy requirements can be reduced considerably in special circumstances. The effective intensity of a light sheet can be increased by sweeping a light beam to form the sheet, thereby concentrating the energy by a factor equal to the height of the light sheet divided by the height of the beam (Kawahashi & Hosoi 1989). This is useful in slowly changing flow fields. Vogel & Lauterborn (1988) achieved a substantially enhanced exposure using forward-scattered light. The object plane is fixed solely by the depth of field. Binnington et al (1983) were able to use a 10-mW He-Ne laser by scattering from 15 to 40 μm TiO_2-coated mica particles into a close-up lens and using ASA 1600 film.

Photographic multiple framing can be done using autowinding cameras

at a few frames per second, cinematic cameras at 30 frames per second, and high-speed cameras at rates of up to several million frames per second. Standard video-imaging rates are 30 frames per second, but high-speed videos with frame rates up to 80,000 per second are available. The very high speed cameras, either photographic or videographic, produce a small number of frames, so they cannot be used to film evolution of a flow field over a long period of time.

RECORDING MEDIA   The principal difference between film and video is spatial resolution. Standard video tubes and video arrays offer about 500×500 pixels, and high-resolution video arrays are available with 2048×2048 pixels. They are currently expensive and relatively slow. Film, on the other hand, offers much higher resolution. A standard 35-mm frame of 300 lines per millimeter Kodak Technical Pan, for example, contains $10,500 \times 7500$ pixels, and a 100 mm $\times$ 125 mm frame of portrait format contains $30,000 \times 37,500$ pixels. We shall see that this additional resolution leads to approximately 10 times better spatial resolution *and* 10 times better accuracy, relative to a standard video camera. Thus, film tends to be used for high-resolution and wide dynamic velocity range measurements of fluids, whereas video recording is suitable for lower resolution, lower accuracy flow measurements, for higher accuracy measurements over smaller fields of view, or for measurements of large particles in two-phase flow. Undoubtedly, video resolution will continue to improve, and it is not unduly optimistic to anticipate that electronic photography may someday offer resolution comparable to chemical photography. In the meantime, researchers seeking the best performance will have to use photography.

Other two-dimensional recording media include photorefractive crystals (Collicott & Hesselink 1987) and thermoplastic films. Stereoscopic recording using several cameras and viewing directions and holographic recording offer the possibility of making three-dimensional measurements. These media are discussed in a later section.

Resolution of Particle Motion

The accuracy of velocity measurements depends upon one's ability to determine the displacement of the particle, Δx, over a certain time interval from measurements of the displacement of the image, ΔX. Assuming, for simplicity, one-dimensional motion and paraxial recording, we have $\Delta X = M\Delta x = Mu\Delta t$ and

$$\frac{\sigma_u^2}{u^2} = \frac{\sigma_{\Delta x}^2}{\Delta x^2} + \frac{\sigma_{\Delta t}^2}{\Delta t^2}, \tag{20}$$

where σ^2 denotes the mean square value of the error in measuring the subscript quantity.

The displacement Δx is uncertain owing to errors in locating the appropriate reference points on the particle images used to mark the beginning and end of the displacement. The reference point is usually taken to be the centroid of an image, but displacement of the centroid may not give the true particle displacement if the particle rotates, or deforms, or if its image changes in any other way during Δt. Errors in locating the centroid arise from the irregular shape of the image, finite resolution due to recording the image on film of finite grain size or on a video detector array of finite pixel size, and/or noise in the electronic readout of the video camera. For most of these errors the rms value of Δx is proportional to the length of the image given by the sum of the recorded image diameter d_τ and the blur due to particle translation during the pulse:

$$\sigma_{\Delta x} = c(d_\tau + M\sqrt{u^2 + v^2}\,\delta t). \tag{21}$$

The uncertainty in Δt and the blur depend upon the light source, but this is usually small unless the flow speed is very high. Assuming negligible timing error, Adrian (1986a) has shown that the error in velocity measurement obeys a type of *uncertainty principle*, i.e.

$$\sigma_u \Delta x_{max} = c u_{max} d_\tau, \tag{22}$$

wherein $\Delta x_{max} = u_{max}\Delta t$ is the spatial uncertainty in the location of the velocity measurement, fixed by the maximum velocity range spanned by the instrument. For given u_{max}, the uncertainty is minimized by minimizing both the image diameter d_τ and the uncertainty in locating its centroid, represented by c.

LOW-IMAGE-DENSITY PIV

Principles

In the low-image-density limit, the mean number of particles per interrogation cell is small ($N_1 \ll 1$). This concept can be applied to systems that do not employ an interrogation spot if we replace the volume of the interrogation cell, $\pi d_1^2 \Delta z_o / 4M^2$, with the volume $|\Delta \mathbf{x}|^3$ defined by the particle displacement, which is always appropriate because $|\Delta \mathbf{x}|$ must be less than Δz_o and/or d_1/M. The implications of low image density are threefold. Firstly, the number of images per unit volume to be processed is relatively small, so that one can afford, computationally, to perform many image-processing operations on each image individually. This is especially important in regard to image-pairing procedures, since the number of pairs is proportional to the square of the number of images. Secondly, there is a low probability of images overlapping in the same interrogation spot. The

probability of one particle in the interrogation volume is $N_1 e^{-N_1} \sim N_1$. Thirdly, the particles and hence the velocity measurements are randomly located. The mean spacing between nearest neighboring particles in the volume is given by $0.55 C^{-1/3}$, and the mean spacing of images in a light sheet is $(4C\Delta z_0)^{-1/2}$.

Image processing is used both to improve the signal-to-noise ratio of the particle images relative to the background and to locate the images. Typical signal-enhancement steps begin with a histogram analysis of the gray levels and a noise-filtering operation to attenuate noise in the background or to remove the noise pixels that can be identified by their low levels in the histograms. The contrast can be enhanced by subtracting a mean level and amplifying the bright pixels to the full-scale value ("histogram slide and stretch"), and a threshold level can be set in order to locate the edges of the particle images in terms of a maximum gray level gradient criterion or a level found from the histogram analysis. The image field can be binarized by setting each pixel whose gray level exceeds the certain threshold equal to one and zeroing all others. Following image enhancement and edge detection, the centroid of each image can be located. The results of performing edge detection on some particle-streak images are shown in Figure 8. Various procedures are described by Dimotakis et al (1981), Hesselink (1988), Perkins & Hunt (1989), Adamczyk & Rimai (1988) and Kobayashi et al (1985). See also Pratt (1978).

Single-Frame Techniques

The simplest single-frame method is streak photography, which is accomplished by time exposing particles in a light sheet over a long time Δt (Figures 7, 8). It can be viewed as a single, long-pulse technique or as the limit of a large number of multiple pulses. It is an excellent method for quantitative visualization of two-dimensional flow fields, but in three-dimensional fields, foreshortened image streaks are created when particles enter or leave the light sheet during the exposure, yielding low measurements.

Several important aspects of PIV can be illustrated by considering the probability of making a successful measurement of velocity from a particle streak. To be successful, the particle streak must not be truncated, and it must not be obscured by overlapping with another streak. Truncation will not occur if the particle lies in a sheet of thickness $\Delta z_0 - |w|\Delta t$, where w is the out-of-plane velocity. The probability of *not* being truncated is given by

$$F_0(w\Delta t) = \begin{cases} 1 - \dfrac{|w|\Delta t}{\Delta z_0}, & |w|\Delta t < \Delta z_0 \\ 0, & |w|\Delta t > \Delta z_0 \end{cases}. \qquad (23)$$

Contours of pathlines

(a) intersecting
    pathline

(b) pathline of
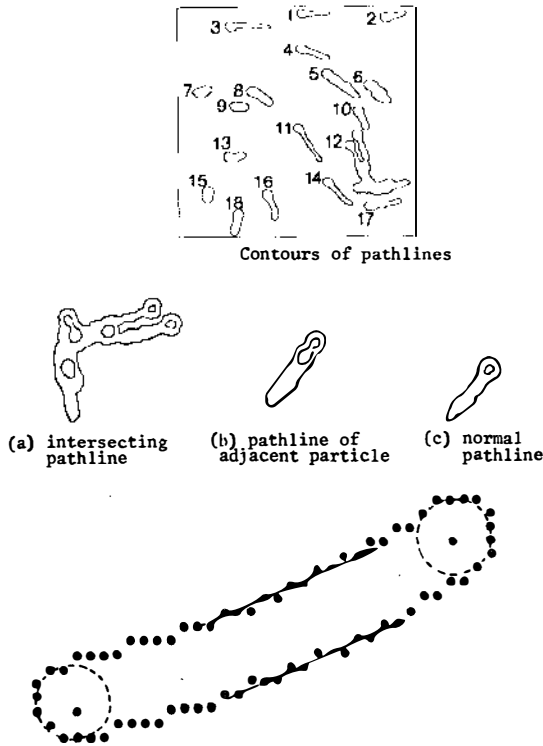   adjacent particle

(c) normal
    pathline

Figure 8 Edge detection of particle streaks. (*Top*) Path lines of 18 fluorescent particles (reproduced with permission from Kobayashi & Yoshitake 1985); (*bottom*) digitization of the streak of a particle illuminated by a long pulse (reproduced with permission from Kobayashi et al 1985).

With reference to Figure 9, the particle streak will not be obscured if there is no other particle in the volume V_t at time t and no other particle enters V_t during the interval $(t, t + \Delta t)$. The latter event is guaranteed if at time t there are no particles in the volume $V_{in} = \int_{in} \mathbf{u} \cdot d\mathbf{s}$ that is swept into V_t during $(t, t + \Delta t)$. The probability of an untruncated, unobscured streak given the velocity $\mathbf{u}$ is then equal to

$$\text{Prob \{unobscured and untruncated} | \mathbf{u}\} = F_o e^{-CV_t} e^{-CV_{in}}. \qquad (24)$$

If the fluid velocity is constant and the diameter of the particle image is d_τ, the diameter and streak length projected back into the fluid are d_τ/M and $|\Delta \mathbf{X}|/M$, respectively. It then follows that
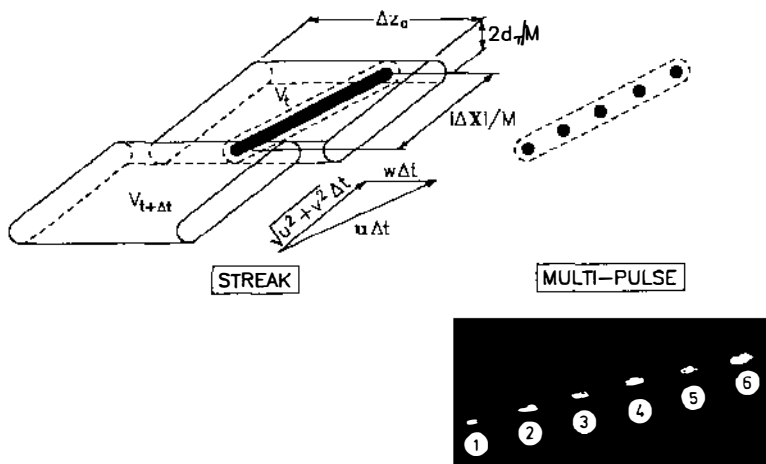
Figure 9   (*Top*) Particles in V_t would obscure the streak produced by the first particle. $V_{t+\Delta t}$ is the material volume that will occupy V_t at time $t+\Delta t$, corresponding to part of the fluid swept into V_t. (*Bottom*) Multiple pulse exposure (reproduced with permission from Cenedese & Paglialunga 1989).

$$V_t = \left(\frac{\pi d_\tau^2}{M^2} + \frac{2d_\tau|\Delta\mathbf{X}|}{M^2}\right)\Delta z_o, \tag{25}$$

$$V_{in} = \left(1 + \frac{|w|\Delta t}{\Delta z_o}\right)V_t - \frac{\pi d_\tau^2 \Delta z_o}{M^2}. \tag{26}$$

The mean number of streaks per unit area times the fraction that are untruncated and unobscured is

$$C\Delta z_o F_o \exp\left[-C(V_t + V_{in})\right].$$

Maximizing this quantity defines an optimum concentration equal to

$$C_{opt} = (V_t + V_{in})^{-1}, \tag{27}$$

where the maximum number of streaks per unit area is

$$N_{opt} = e^{-1}\Delta z_o F_o (V_t + V_{in})^{-1}. \tag{28}$$

This simple analysis of the streak method reveals many characteristics that recur throughout PIV. Equations (24)–(26) show that the probability of detection decreases exponentially with Δz_o and $|w\Delta t|$, which explains the rationale for using thin light sheets and the desirability of minimizing the out-of-plane velocity component (possibly by the proper choice of the light-sheet plane or by restricting the method to two-dimensional flow). In

general, the detection probability and the optimum concentration are increased by reducing V_t or V_{in}; this can be done by reducing (a) the image diameter, (b) the length of the streak, or (c) the depth of the light sheet. Ideally, the detection probability should be close to unity and independent of the velocity, for dependence on the velocity implies statistically biased sampling. In fact, *the sampling probability is biased toward small velocities,* as particles with such velocities suffer less loss of pairs owing to out-of-plane motion, and they sweep out smaller volumes. This bias must be minimized by appropriate choice of parameters.

Unfortunately, small displacements that reduce V_t and V_{in} also lead to low accuracy. These opposing trends can be balanced to yield satisfactory results if very small images are used. However, most applications of streak photography use light sources that are not strong enough to produce good exposures of very small particles, and the tendency is for streak photography to use particles of size larger than 50–100 μm. This is quite satisfactory for two-phase flow, but it is not ideal for fluid measurements.

Multipulse methods are similar to streak photography in the sense that the chain of images usually defines a relatively long, nearly continuous particle trajectory. Figure 9 (*bottom*) is an example of a multipulse photograph. As suggested by the drawing in Figure 9 (*top*), the multipulse images can be approximated as a streak of the same length for the purposes of evaluating the sampling probability. Thus, the multipulse technique is subject to considerations similar to those discussed for particle streaks, although the quantitative effects are ameliorated to a small extent by the smaller area occupied by the multipulse image. In particular, it is beneficial to minimize the image diameter and the streak length to reduce the probability of overlap.

In general, the multipulse code may consist of a series of long and short pulses or irregularly spaced pulses, permitting easy determination of the direction of motion (Agui & Jiménez 1987, Adamczyk & Rimai 1988). Beginning and ending the code with dots yields measurements that are significantly more accurate than streak codes, because the centroid of a dot can be located more accurately than the end of a streak. Multipulse dot codes also provide significant relief from the out-of-plane bias effect if one does not insist on measuring the length of the entire dot pattern when it is truncated by the particle entering or leaving the light sheet. Switching from an n-dot pattern to an $n' < n$-dot pattern has the effect of reducing the Δt that is used, thereby increasing the function $F_o(w\Delta t)$.

An important advantage of multipulse PIV over streak recording is the concentration of light energy into pulses, resulting in bright dot images if the light source is a pulsed laser or flash lamp that achieves high pulse intensity by concentrating the energy into a short pulse. Hence, smaller

particles can be used, allowing more accuracy and higher data density. Chopped continuous sources do not enjoy this benefit; moreover, as the flow rate and the chopping rate increase, the pulse duration and hence the energy per pulse decrease in inverse proportion, limiting these light sources to relatively slow flows and/or large particles unless the detector is very sensitive, such as for a video camera enhanced by a silicon intensifier tube (SIT).

An example of a velocity vector field in a water-channel flow measured with a four-pulse, stereo camera pair and 0.1–0.5 mm polystyrene particles is shown in Figure 10 (Utami & Ueno 1984; cf also Utami & Ueno 1987). These results illustrate the randomness of the locations of the velocity vectors and the maximum data density that one typically expects with low-image-density PIV. Other examples of single-frame/multipulse PIV are found in the work of Khalighi (1989), Agui & Jiménez (1987), Braun et al (1989), and Willis & Deardorff (1974).

Single-frame/double-pulse PIV has been studied in the low-image-density limit by Landreth et al (1988). The use of only two pulses requires special procedures to identify the direction of motion, and it makes the pairing of images more difficult. Adrian (1986b) proposed an image-shift-
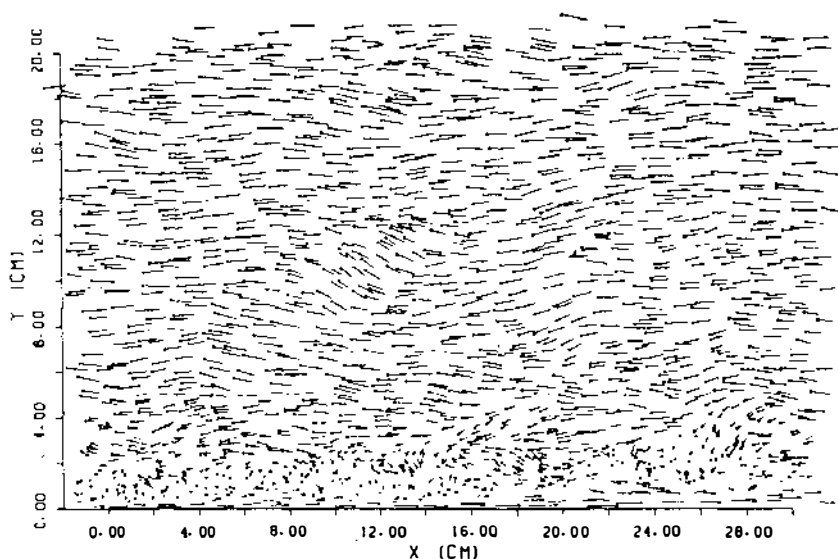

Figure 10 Turbulent open-channel water-flow field measured by multipulse low-image-density PIV (reproduced with permission from Utami & Ueno 1984).

ing technique that resolves the directional ambiguity inherent in a two-dot record by optically shifting the image field between first and second exposures to introduce an offset that exceeds the largest negative value of one of the velocity components. In this way, the *image* displacements are always positive, and negative *particle* displacements are inferred by subtracting the imposed shift from the positive measurements. Shifting can be performed by photographing the fluid through a rotating mirror (Landreth et al 1988) or by using a birefringent crystal in front of the camera to shift the image field when the polarization of the scattered light is switched from the first pulse to the second pulse (Landreth & Adrian 1988). Very rapid and precise shifting can be achieved with this technique.

Interrogation procedures for low-image-density PIV make use of the fact that the probability of images from different particles overlapping is low because the particle spacing is large compared with the particle displacement. Landreth et al (1988) assumed that if an interrogation spot contained two images, the images belonged to the same particle. Requiring exactly two images gave a data yield of about 0.1 velocity samples per square millimeter when the interrogation spot was 1 mm^2 and the image density was 0.5. The pairing assumption failed in about 20% of the measured vectors, resulting in bad measurements that had to be removed by postinterrogation processing of the vector field. The latter procedure removed vectors that were substantially different from the locally averaged vector field. Following this approach, however, Landreth et al were unable to obtain fields containing over 2000 vectors in a turbulent-jet flow.

A somewhat different procedure is the *nearest neighbor* approach, in which each particle image is paired with its nearest neighboring image. Given an image from a particle in a light sheet, the probability that its nearest neighbor is its second image equals the probability that it remains in the light sheet at the time of the second exposure, $F_o(w\Delta t)$, times the probability that there are no other particles in a cylinder of height Δz_o and radius $\sqrt{u^2+v^2}\Delta t$ at time t, and that there are no other particles in this same control volume at $t+\Delta t$. Assuming a Poisson distribution, the probability can be shown to be

Prob {nearest image is true second image given **u**}

$$= F_o(w\Delta t)\exp[-(2-0.53F_o)C\Delta z_o\pi(u^2+v^2)\Delta t^2]. \quad (29)$$

To evaluate the unconditional probability, this equation must be averaged over the fluid velocities in the flow field. The successful detection rate per unit area is the number of images per unit area times this probability.

We see that, as in the case of the streak-image technique, the probability of obtaining a correct pair by this procedure can be made high by restricting

Δt, so that the out-of-plane displacement is a small fraction of Δz_o, and the in-plane displacement $\sqrt{u^2+v^2}\Delta t$ is small compared with the mean image spacing $(4C\Delta z_o)^{-1/2}$. Small displacements give good spatial resolution but poor accuracy, unless the diameters of the particle images are small. In Landreth et al (1988) the displacements were less than 0.5 mm and images less than 15 μm were obtained using a contact printing procedure described by Pickering & Halliwell (1984). Accuracy was of the order of 0.4–1% of the full-scale velocity.

Multiframe Techniques

The simplest application of multiframing is to sample the velocity field at a periodic sequence of times with frame interval T_f, each sample consisting of a single, double, or multipulse exposure of the type discussed in the previous section. In these methods the time between exposures (Δt) that is used to measure the velocity is independent of the time between velocity samples (T_f). This is advantageous because Δt can be selected according to the velocity and the requirements of spatial resolution, whereas T_f can be chosen to follow the evolution of the flow, as determined by its inherent time scales. Khalighi (1989) reports measurements of this type in which he followed the development of the intake swirl in an engine using multipulse exposures recorded on successive frames of a video camera.

Multiframe/single-pulse methods are essentially conventional cinematography and video recording of single exposures in each frame. The advantages of this approach are (*a*) the images of each exposure are isolated, eliminating confusion that results from superposing fields on single frames; (*b*) the particles can be tracked for long times; and (*c*) the direction of motion is fully determined (Perkins & Hunt 1989). The principal disadvantage of this approach is that Δt is now constrained to be equal to T_f or an integral multiple, and this constraint confines measurements to low speeds if one uses standard 30-Hz video and cinematic frame rates. If the maximum desirable displacement is 1 mm, the maximum allowable velocity is only 30 mm s^{-1}. Of course, higher speed cameras are available, but at very high speeds they produce a limited number of frames.

The reduced confusion that results from nonsuperimposed images makes it possible to achieve more reliable computer pairing of the images. Various procedures have been developed for tracking images from one frame to the next. Frieden & Zoltani (1989) describe a nearest neighbors approach, and Perkins & Hunt (1989) and Uemura et al (1989) detail automated algorithms that involve cross correlation of groups coupled with individual pairing. Both groups report processing times of order 10–40 s per video frame containing several tens or hundreds of particles using a personal computer. Perkins & Hunt (1989) use results over many frames

to track Lagrangian trajectories in two-phase flows. An example of their experiment on the motion of large particles in a cylinder wake is shown in Figure 11. They estimate the error rate in matching particles to be 1–2%. Guezennec & Kiritsis (1989) describe a similar algorithm in which the velocity field in a large region is estimated by cross correlation of the images, and then the images in the first frame are projected onto the second frame using this estimate. Pairing is done by a nearest neighbors criterion that is obviously better than nearest neighbors without a priori displacement information because the displacement estimate reduces the allowable domain in which the second image can reside.

Three-dimensional, low-image-density PIV is usually performed with multiframe recording, although there is no insurmountable reason why it cannot be done with single-frame exposures. Chang et al (1984) have described pattern-matching techniques for stereo cinematic photographs of approximately 100 particles in a turbulent mixer, and more recently Nishino et al (1989) have also automated the analysis of three video views of 280-μm particles in decaying turbulence in water using a 10-Hz videoframe rate. The observed volume is 5 cm × 5 cm × 5 cm, and they were able to measure 100 vectors out of approximately 600 images recorded in each frame. The point positions indicated by the cameras were calibrated

Figure 11 Trajectories of particles in a cylinder wake measured by multiframe/single-pulse recording and image tracking (reproduced with permission from Perkins & Hunt 1989).

and fit to a representation developed by Murai et al (1980) for cameras with arbitrary orientation and lens distortion. Related work is reported by Racca & Dewey (1988), who use orthogonal views, and Kent & Eaton (1982).

As noted earlier, stereoscopic photographic recording of three-dimensional volumes requires large depth of field, which in turn requires low photographic resolution [cf Equations (5) and (7)]. The relatively large particles used by Nishino et al (1989) are symptomatic of these requirements and are consistent with the resolution provided by a video camera.

Higher resolution in three-dimensional volumes can be achieved by using holographic recording because the depth of the hologram is much larger than the depth of field of a lens. Further, the point response of a hologram is inversely proportional to the size of the holographic plate, and the size is often many times larger than the feasible aperture of a lens, yielding improved resolution (Akbari & Bjelkhagen 1986).

High-speed holographic/cinematic recordings have been proposed by Weinstein et al (1985) using a system in which a copper-vapor laser operates at less than 2 kHz and illuminates 40-μm particles in water to form sequences of in-line holograms that are recorded on a 35-mm high-speed film transport. Three-dimensional particle positions are located accurately by using two orthogonal holographic views. The particle-image fields in a given frame are reconstructed and viewed with a video camera mounted on an XYZ controller to scan the fields and locate the particle centroids. Tracking is performed from frame to frame. It is understood that the results of this project will be forthcoming shortly.

Haussmann & Lauterborn (1980) and Zarschizky & Lauterborn (1983) have also used high-speed holographic techniques to record the fluid fields and motions of bubbles in cavitating flows. Rates of 67,700 holograms per second were achieved.

HIGH-IMAGE-DENSITY PIV

Principles

High-image-density PIV uses particle concentrations large enough to ensure that every interrogation spot contains many images. In the limit $N_I \gg 1$ the probability of finding no particles in a spot [given by $\exp(-N_I)$] is very small. In practice, values of $N_I > 5$–10 produce asymptotically large behavior.

High-image-density PIV is usually performed with single-frame recording on photographic film for the purposes of providing maximum resolution in space and velocity. The particle images must be small, typically of order 10–25 μm, to avoid filling the interrogation spot whose size is less

than a few millimeters, and to give accurate measurements when the displacements are small. Typical displacements are 10 μm to a few millimeters. The field of view is often a 25 mm × 35 mm frame, but 100 mm × 125 mm frames containing several tens of thousands of interrogation spots are also used. A section of a single-frame/double-pulsed high-image-density photograph is shown in Figure 12.

Multiple-exposed single frames are preferred over single-exposed multiframes because the inaccuracy of registering separate frames over a large field of view can cause severe errors. For example, 0.1% shrinkage of a 100-mm frame produces spurious displacement of images in that frame relative to those in another frame as large as 100 μm. This can be a large fraction of the total displacement. On the other hand, multiple exposures on the same film frame are automatically registered with respect to each other, and any registration error refers to the *location* of the measurement, not the displacement.
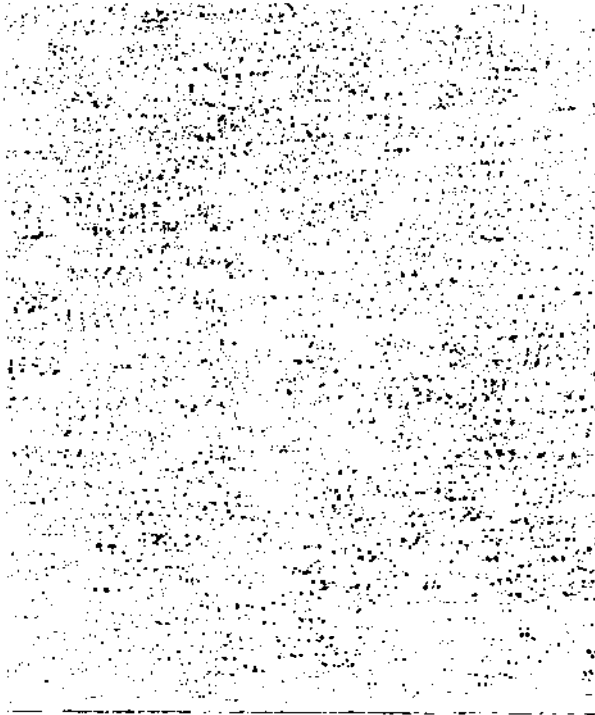

Figure 12 Single-frame/double-pulsed photograph of 5-μm Al$_2$O$_3$ spheres in a turbulent water channel. Mean flow is from left to right.

Exposures may be double pulses or multiple pulses, but unless otherwise stated, the following discussions pertain to the double-pulsed case.

The primary consequences of high image density are that almost every interrogation cell contains enough particles to yield a measurement, and that the large number of images makes it difficult to track individual particles. The types of interrogation-spot images that must be processed are illustrated in Figure 13. The left-hand column contains images of 1 mm × 1 mm interrogation spots located at different points in an impinging vertical jet flow. Figure 13*a* is from a spot located in a region of nearly
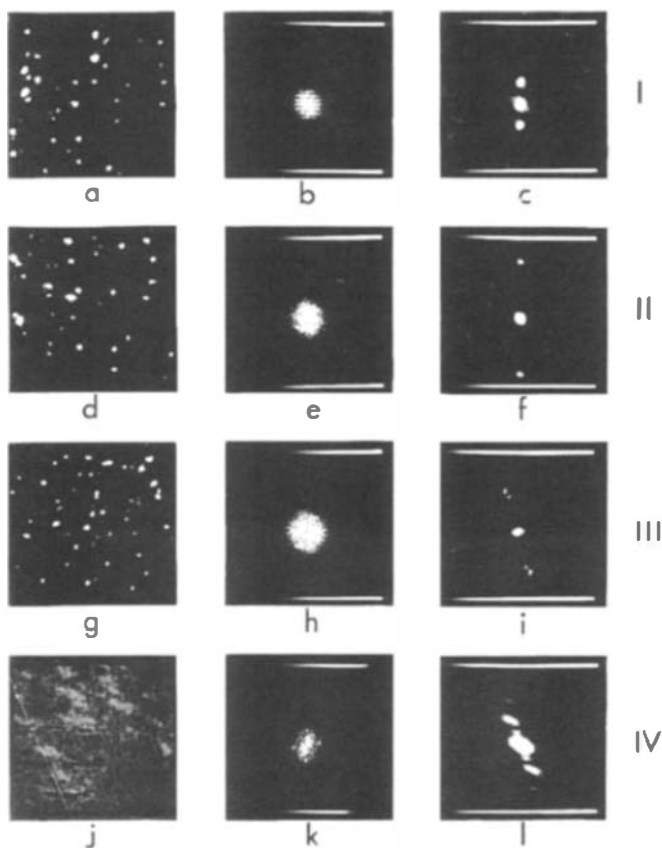

Figure 13 Sample interrogations of 1 mm × 1 mm spots digitized with a 256 × 256 video array. (*a,d,g,j*) Image fields of the interrogation spots; (*b,e,h,k*) fringe patterns resulting from Fourier transforms of the image fields; (*c,f,i,l*) correlation patterns resulting from Fourier transforms of the fringe patterns (reproduced with permission from Landreth & Adrian 1989).

uniform, slow vertical velocity, whereas the spot in Figure 13*d* is from a region of larger vertical velocity. Figure 13*g* is from the shear-layer region of the jet, where the horizontal gradient of the vertical velocity was large, and Figure 13*j* is from a corner of the photograph, where the lens distortion produced very poor images. The image density in these spots is about $N_I \cong 20$.

Knowing that the velocity is vertical, it is easy for one to see the pairs of images in Figure 13*a*, but not so easy in Figure 13*d*. The gradient in Figure 13*g* makes pairing by eye quite difficult, and the poor quality of images in Figure 13*j* makes it impossible. The challenge of image interrogation is to design computer algorithms that will measure the displacements of images in such spots accurately, reliably, and with a minimum amount of human intervention.

The methods of interrogation that are currently in use are primarily statistical approaches that probabilistically infer the proper pairings and measure the average displacement of the group of particles in the interrogation cell. The speed of interrogating a spot is an important issue, as each photograph contains thousands of spots. Several of the methods that are used are discussed next.

Interrogation Techniques

As shown in Figure 4, interrogation of a photograph begins by illuminating an interrogation spot with a beam of intensity $I_I(\mathbf{X} - \mathbf{X}_I)$, where $\mathbf{X}_I$ is the center of the spot. The interrogation spot intensity is given by

$$I(\mathbf{X}) = I_I(\mathbf{X} - \mathbf{X}_I)\tau(\mathbf{X}), \tag{30}$$

where $\tau(\mathbf{X})$ is the intensity transmissivity of the photographic image.

If the images are recorded on a video frame instead of a photograph, the interrogation spot can be defined digitally by multiplying the data in the frame array by a window function whose shape corresponds to I_I. Since the parallels between video recording and photographic recording are generally obvious (except for noise effects, such as film grain and electronics readout noise), we shall discuss interrogation in terms of photographic recording only.

DIRECT AUTOCORRELATION   The autocorrelation of $I(\mathbf{X})$ is given by

$$R(\mathbf{s}) = \int_{\text{spot}} I(\mathbf{X})I(\mathbf{X} + \mathbf{s})\, d\mathbf{X}, \tag{31}$$

where $\mathbf{s}$ is a two-dimensional displacement vector. The third column in Figure 13 shows $R(\mathbf{s})$ for each of the interrogation spots in the first column. Where $\mathbf{s} = 0$, there is a strong self-correlation peak R_p, corresponding to

each image correlating with itself. Where **s** equals the mean displacement, there is a second peak R_{D+}, called the positive *displacement* peak, that corresponds to first images correlating with second images. An identical peak R_{D-} occurs at the negative value of the mean displacement, corresponding to second images correlating with first images. In addition to the self-correlation peak (which conveniently defines the origin) and the two strong displacement peaks, there are a number of noise peaks resulting from random overlap of particle images in the $I(\mathbf{X})I(\mathbf{X}+\mathbf{s})$ product.

The velocity is determined by locating the centroid of the tallest peak in the correlation plane (other than the self-correlation peak). If the tallest peak is the positive displacement peak with centroid $\boldsymbol{\mu}_{D+}$, the velocity is estimated from

$$\boldsymbol{\mu}_1 = \boldsymbol{\mu}_{D+}/M\Delta t. \tag{32}$$

The measured centroid contains, of course, a random component that depends upon the distribution of particles and the correlation noise. It has been shown (Adrian 1988) that the expected value of the centroidal velocity estimation is a volume average of the velocity in the interrogation cell, i.e.

$$\langle \boldsymbol{\mu}_1 | \mathbf{u} \rangle = \frac{\displaystyle\int \mathbf{u}(\mathbf{x}, t) W \, d\mathbf{x}}{\displaystyle\int W \, d\mathbf{x}}, \tag{33}$$

where W is a weighting function given by

$$W = I_{o1}(\mathbf{x})I_{o2}(\mathbf{x} - \mathbf{u}\Delta t)I_1(M\mathbf{x} - \mathbf{X}_1)I_1(M\mathbf{x} + M\mathbf{u}\Delta t - \mathbf{X}_1). \tag{34}$$

Here I_{o1} and I_{o2} are the intensities of the first and second light sheets. The dependence of W on **u** defines a measurement volume whose size is biased toward low-velocity particles that have less chance of leaving the light sheet and/or the interrogation spot. This *velocity bias* is zero if the velocity is uniform, and it is small if the velocity variation across the measurement region is small, i.e. if the spatial resolution is adequate.

The strength of the displacement correlation peak is proportional to the number of particle-image pairs in the interrogation cell. This number is proportional to N_1, decreased by the fraction of second images that leave the cell due to out-of-plane motions and by the fraction lost by in-plane motion. For uniform flow with velocity **u**, the mean of the displacement correlation evaluated at its peak value is (Keane & Adrian 1990)

$$\tfrac{1}{2}R_p(\mathbf{0})F_o(w\Delta t)\exp[-4|M\mathbf{u}\Delta t|^2/(d_1^2 + d_\tau^2)],$$

where F_o represents the out-of-plane loss of pairs, and the exponential

function represents the in-plane loss of pairs. [Note the similarities with Equation (29).] Hence, the large velocities reduce the amplitude of the signal peak.

If one of the noise peaks exceeds the positive displacement peak, it will be identified incorrectly as the signal peak, and an invalid measurement results. To reduce the probability of invalid measurements, one can require that the ratio of the tallest peak (excluding R_p) to the next tallest exceeds a prescribed *detection threshold*. One can also restrict the search for the tallest peak to a region in the s-plane in which the vector is expected to be located, on the basis of consistency with neighboring measurements, or one can accept invalid measurements during interrogation and clip them out of the vector data file in a postinterrogation procedure that compares each vector with its neighboring vectors (Landreth & Adrian 1989). At the same time, the second, third, and fourth tallest peaks can be evaluated to see if they would yield vectors more consistent with the neighboring field.

In any measurement procedure, the displacement correlation peak becomes smaller and less likely to be detected as the velocity increases. We refer to this bias against high velocities as *velocity bias*. In low-image-density PIV, it biases all measurements. In high-image-density PIV, velocity bias is much less severe because the loss of image pairs does not cause a measurement failure if the number of remaining pairs is large enough. Thus, the fraction of successful measurements asymptotically approaches 100% as N_I becomes large and $|\Delta X|/d_I$ is made small.

Theoretical analysis and extensive numerical simulations (Keane & Adrian 1990) show that the performance of the double-pulsed auto-correlation technique is optimized by the following approximate criteria:

$$N_I > 10-20,$$

$$\sqrt{\overline{u^2+v^2}}\Delta t < \tfrac{1}{4}d_I/M,$$

$$w\Delta t < \tfrac{1}{4}\Delta z_o,$$

$$|\Delta \mathbf{u}|/|\mathbf{u}| < 0.2,$$

where $|\Delta \mathbf{u}|$ is the velocity variation over the measuring volume due to local gradients. By satisfying these constraints, it is possible to make valid measurements in over 90–95% of the interrogation spots with small bias errors.

The use of multiple pulses separated by Δt improves the strength of the displacement correlation by increasing the number of correlated pairs of images. For example, a four-pulse single exposure containing N_I particles, none of which leave the volume, would produce a self-correlation peak of height $4N_I$, a first correlation peak at $\mathbf{s} = M\mathbf{u}\Delta t$ that is $3N_I$ high, a second

peak at $2M\mathbf{u}\Delta t$ that is $2N_1$ high, and a third peak at $3M\mathbf{u}\Delta t$ that is N_1 high. The performance is much the same as for a double-pulse image from $3N_1$ particles using the same Δt. If the four-pulse exposure were obtained by reducing Δt by three to maintain the same total distance from beginning to end, then the first correlation peak would be more detectable but less accurate.

DIRECT CROSS CORRELATION   The loss of pairs due to in-plane motion out of the interrogation spot can be eliminated by performing cross-correlation between first images in a small, *first interrogation window* and second images in a larger, *second interrogation window*. The procedure is very similar to that described by Landreth et al (1988), except that searching the second window for a second image is replaced by cross-correlating all images. The second window is chosen on the basis of a priori knowledge about the flow field, such as a predominant mean flow, an imposed image shift, or an estimate of the local flow direction based on neighboring vectors. Similarly, a priori knowledge of the out-of-plane component can be used to locate the second light sheet in a plane that will capture most of the second images, as in Lee et al (1989). Cross correlating images in a first interrogation cell with those in a second cell will increase the strength of the correlation peak and thereby increase the probability of making valid measurements. More work is needed in this area.

YOUNG'S FRINGES   The Young's fringe method has been used more widely than any other technique for interrogation of high-image-density photographs. As shown in Figure 4 (*bottom*) a lens is used to perform a two-dimensional Fourier transform of the lightwave from the interrogation spot, and the intensity of the Fourier transform is measured a distance L from the lens. The lens performs an accurate Fourier transform of the phase and the amplitude of the lightwave if it is located one focal length from the film and if the fringe plane is one focal length from the lens (Goodman 1968). Physically, each image acts as a point source whose rays are collimated by the lens into a plane wave propagating at a small angle to the optic axis of the lens. Each pair of images produces a pair of mutually inclined plane waves that interfere to form a Young's fringe pattern oriented perpendicular to the displacement vector between the images. The randomly located image pairs produce fringes with random orientations and spacings that superpose to form a random speckle pattern. The pairs that are separated by the same displacement vector form identical fringes that reinforce each other, thereby creating a dominant pattern.

The fringe pattern in Figure 13b is typical of a pattern from several uniformly spaced pairs. In Figure 13e the small fringe spacing caused by

the large pair spacing makes the fringes difficult to see. The fringes are also difficult to see in Figure 13*h* owing to velocity gradients creating fringes with variable spacing. In Figure 13*k* the poor image quality also obscures the fringes.

Interrogating the fringes involves determining their orientation and their spacing. Numerous one-dimensional techniques have been proposed (cf Meynart 1983c, Kaufman et al 1980, Ineichen et al 1980, Lourenco & Krothapalli 1988). These methods form one-dimensional samples, either by sampling along lines across the fringe pattern or by compressing the two-dimensional Young's fringe pattern into a one-dimensional array using cylindrical lenses or integration. The one-dimensional arrays can be analyzed quickly by Fourier transform or by fringe counting. A variation on the one-dimensional theme forms one-dimensional fringes by using a cylindrical lens to perform a one-dimensional Fourier transform (Collicott & Hesselink 1986).

The most powerful method of analyzing Young's fringes is the two-dimensional Fourier transformation of the fringe-intensity distribution. The transformation can be performed digitally, in which case a video camera digitizes the Young's fringes and a fast Fourier transform (FFT) of the digitized array is then calculated by a computer (Adrian 1986a, Huntley 1986a). It can also be done optically, as is discussed in the next section. The Fourier transform of the fringe intensity equals the Fourier transform of the product of the Fourier transform of the amplitude image field multiplied by the complex conjugate of the Fourier transform of the amplitude of the image field. From the convolution theorem, the Fourier transform of the product is equal to the convolution of the Fourier transforms, or, in other words, the convolution of the *amplitude* of the interrogation-spot image field. As shown in Keane & Adrian (1990), this is only slightly different from the convolution of the *intensity* of the interrogation-spot image field, so that the Fourier transform of the Young's fringe pattern can be analyzed using the same procedures that have been described for the analysis of the two-dimensional correlation function. In particular, the FFT of the fringe intensity will yield a convolution function that contains a self-correlation peak, positive and negative displacement peaks, and noise peaks.

The advantage of the Young's fringe method is that it performs one Fourier transformation optically, with no cost to the total processing time. This is a significant savings that can increase the processing speed by a factor of two. For example, the interrogation system used by Landreth & Adrian (1990) employs a Numerix 432 array processor operating at 30 Mflop to perform a 256×256 FFT computation in 190 ms. In this study, direct digital correlations were computed by digitizing each image spot

onto a 256 × 256 array and digitally performing one real-to-complex FFT, computing the modulus squared of each element in the array and then performing an inverse real-to-complex FFT taking advantage of symmetry. Including the search time for the four tallest peaks, the total time required was 0.45 s per interrogation spot. In comparison, by using a lens in a Young's fringe system to perform the first FFT, the computation time is reduced to 0.3 s per spot.

The advantage of direct imaging is that image processing can be performed on the particle images, including signal enhancement, centroiding, and particle sizing.

Huntley (1989) has compared four methods of Young's fringe analysis: two-dimensional Fourier transform, two-dimensional Walsh transform (Huntley 1986b), one-dimensional integration (Robinson 1983), and one-dimensional autocorrelation (Meynart 1983a). He finds that the two-dimensional Fourier transform gives the lowest error.

Malyak & Thompson (1984) have described a method of forming Young's fringes from recordings of in-line holograms.

OPTICAL CORRELATION   The two-dimensional correlation function of an interrogation spot can be formed optically by replacing the two digital FFT operations with optical Fourier transformations. The generic optical correlator consists of a lens that Fourier transforms the amplitude of the interrogation-spot image, a device that forms the modulus squared, and a second lens that Fourier transforms the modulus squared (cf Goodman 1968). The system is the same as a Young's fringe system up to the fringe plane, at which point the intensity of the fringes must be written onto an optical device that transmits a coherent wave whose amplitude is proportional to the fringe intensity. The transmitted wave is Fourier transformed by a lens to form an optical field whose amplitude is proportional to the correlation function. The intensity of this field is digitized by a video camera, and the usual peak-detection and centroid calculations are done digitally.

Interestingly, the most difficult step in coherent optical correlation is forming a coherent field whose amplitude is proportional to the modulus squared of the first Fourier transform, i.e. the intensity of the Young's fringe pattern. This can be done by photographing the Young's fringes and illuminating the developed photograph coherently, but to develop a photograph for each interrogation spot is clearly too awkward. Arnold & Hinsch (1988) have made this process more feasible by using holographic-imaging elements to form many interrogation spots that can be photographed simultaneously.

Photorefractive crystals such as bismuth silicon oxide (BSO) are capable

of recording an intensity field in the form of a refractive-index variation that can be subsequently erased by changing the electric field applied to the crystal. Coupland & Halliwell (1988) describe a system in which a hologram of the interrogation spot is recorded in a BSO crystal using an off-axis reference beam. When the reference beam is removed, the crystal phase modulates the incident wave to produce a transmitted wave whose amplitude is proportional to the fringe intensity. BSO crystals respond slowly at moderate recording energies. Coupland & Halliwell (1988) report 1 s response at 10 mW cm^{-2}. However, Gheen & Cheng (1988) have demonstrated 1000 times faster response in GaAs:Cr photorefractive compound semiconductors.

Another approach to optical correlation uses a video camera to digitize the intensity of the Young's fringe pattern and then writes the intensity pattern to a medium whose amplitude transmittance is proportional to the write signal. Farrell & Goetsch (1989) have demonstrated the feasibility of using a liquid-crystal TV screen for this purpose, while Kompenhans et al (1989) have done similar feasibility experiments with a Faraday-effect spatial light modulator.

Spatial light modulators and photorefractive crystals currently do not have very fast response times, but these times can be expected to decrease. Ultimately, the speed of optical interrogation methods may be limited by the time required to write the video digitization of the correlation function into a peak-search device and by the peak-search time itself.

The choice between analog optical methods and digital methods is not clear; it will ultimately depend on future technological developments in optical and semiconductor computing. For example, very fast digital-processor boards for two-dimensional FFT calculations are certain to become available, and even using available array processors such as the Numerix device described above, it has been possible to process 3000 vectors per minute with good accuracy by reducing the interrogation-spot pixel resolution to 32×32. At this rate, a grid of 25×35 vectors on a standard 35-mm frame of film can be analyzed in less than 20 s.

Applications

High-image-density PIV has been used to study many flows. Applications have been mainly in water owing to the ease of seeding liquids with scattering particles, but several successful experiments have been performed in airflows, including some in difficult environments. Water-flow studies include the multipulse work of Lourenco & Krothapalli (1987, 1988) on wakes and airfoils, the turbulent thermal-convection experiments of Meynart et al (1987) and Arroyo et al (1988), the impinging wall-jet study of Landreth & Adrian (1990), and studies of wave motion by Gärtner

et al (1986). Kompenhans & Höcker (1988) have been able to make high-image-density PIV measurements in a 360 m s^{-1} air jet.

A sample velocity field from a recent turbulent water-channel flow study by Liu et al (1990) is shown in Figure 14. In this experiment a double-pulsed ruby laser with 2 J per pulse illuminated 5-μm diameter Al_2O_3 spheres whose image density was carefully adjusted to give 10–20 particles per interrogation spot. The measurement volume dimensions were 1.0 mm $\times$ 0.3 mm $\times$ 0.8 mm in the x-, y-, and z-directions, respectively, corresponding to $7.5 \times 2.25 \times 6.0$ in terms of viscous wall units. The rectangular shape of the interrogation cell was chosen to improve the probability of finding pairs in a flow with a strong x-component. (The root-mean-square velocity fluctuation on the centerline of the channel is only 4% of the mean flow.) Photographs like that in Figure 12 were interrogated on a 0.5-mm grid by two-dimensional FFT of the Young's fringe pattern. The flow field contains 12,000 vectors, each accurate to
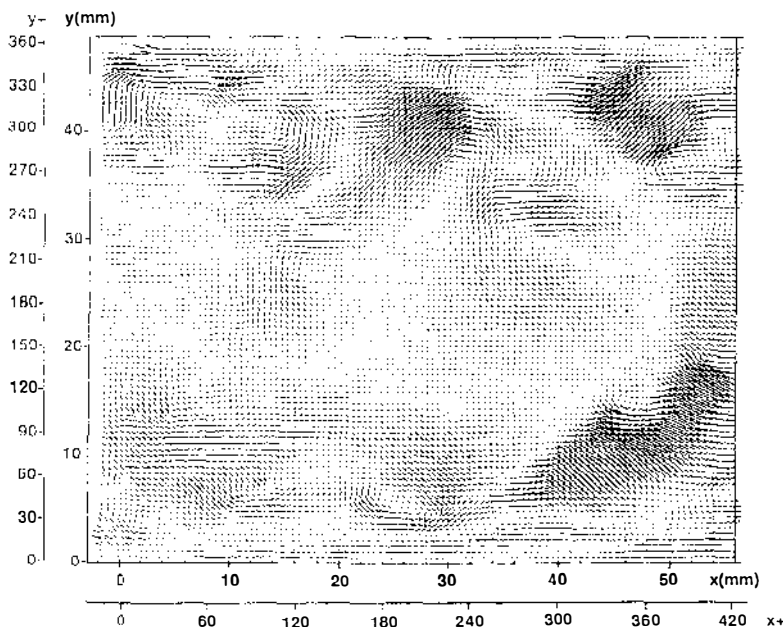
Figure 14 Fluctuating velocity field in turbulent channel flow at a Reynolds number of 2872 based on the half-channel height. The fluid is water (reproduced with permission from Liu et al 1990).

about 1% of the full-scale mean velocity. (The local mean velocity has been subtracted to obtain the fluctuating velocity vectors in Figure 14.)

The density of data in Figure 14 is high enough to permit differentiation to calculate the out-of-plane component of vorticity. The vorticity contours in Figure 15 correspond to the velocity field in Figure 16. Note the concentrations of vorticity in shear layers close to the walls. Statistics of the turbulent flow have been calculated by averaging along lines of constant y and ensemble averaging over 11 photographs. Mean-velocity profiles calculated in this way are plotted in the usual wall variables U^+ and y^+ in Figure 16 and compared with LDV measurements and direct numerical simulations. The agreement is encouraging.

High-quality airflow measurements can be performed by PIV if care is taken to ensure adequate concentrations of the appropriate scattering particles. Measurements of grid turbulence in a large, relatively high-speed wind tunnel have been reported by Höcker & Kompenhans (1989). They used 1-μm oil droplets. Reuss et al (1989) performed measurements in a motored research model of an internal combustion engine using the reaction of $TiCl_4$ with water vapor to produce TiO_2 particles in the 1–2 μm range.

In addition to its applications to turbulent flows, PIV is very useful in the study of flows with complex geometries. Paone et al (1989) have, for example, measured fields in the passageways of a centrifugal pump impeller.
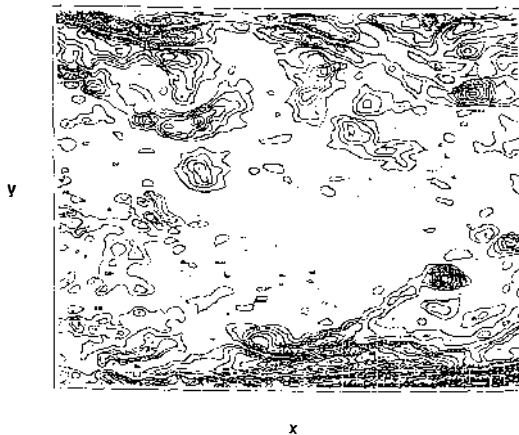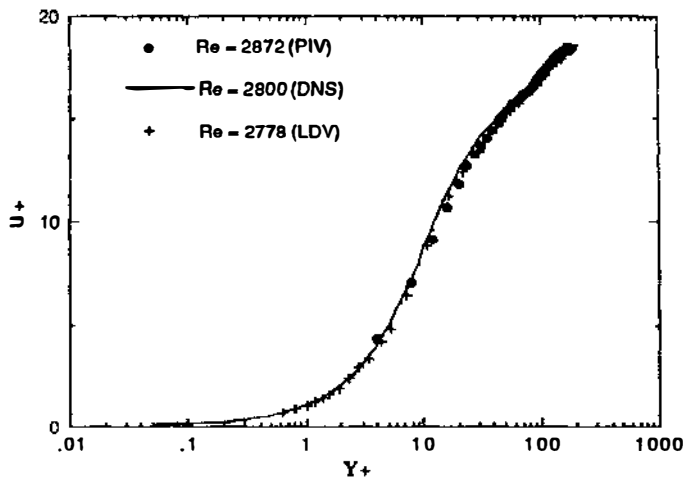
Figure 15 Contours of the z-component of vorticity found by differentiating the vector field in Figure 14 (reproduced with permission from Liu et al 1990).

Streamwise mean velocities

Figure 16   Mean-velocity profile in the turbulent channel flow calculated from an ensemble of 11 PIV photographs. The comparison is with LDV data and direct numerical simulations (reproduced with permission from Liu et al 1990).

CONCLUDING REMARKS

Particle-image velocimetry has developed rapidly during the last decade. It is now clear that the basic two-dimensional technique is capable of providing accurate, high-quality measurements of instantaneous fields in a variety of laboratory-scale flows of gases and liquids spanning the range from millimeters per second to several hundred meters per second. Interrogation methods depend upon the image density, with the greatest demands for interrogation time coming from high-density photographs. The computation time required to process a photograph is now reasonable using appropriate laboratory computers, and the computation needed to process a single low-image-density video frame can be handled by relatively small computers. As the analysis of the images becomes less demanding, one can anticipate extensions of the technique to measurements involving hundreds or even thousands of frames of data. In particular, cinematic recording of vector fields, stereographic recording, and holographic recording are generalizations that will become more common as processing times decreased.

Interrogation techniques will continue to evolve, although the two-dimensional correlation and two-dimensional FFT techniques are already so good that major improvements in the data yield and the data reliability arc not to be expected. Work is needed to relate measurements to the actual flow field in greater detail and to develop methods of interrogating regions of very rapid velocity variation with high reliability.

One of the most welcome capabilities offered by PIV is the measurement of vorticity and rate-of-strain fields. These quantities are as fundamental to fluid mechanics as the velocity field itself, but they have been largely absent from the experimentalist's vocabulary owing to the difficulties in measuring derivative quantities even on a point-wise basis.

ACKNOWLEDGMENTS

Literature Cited

Adamczyk, A. A., Rimai, L. 1988. 2-Dimensional particle tracking velocimetry (PTV): technique and image processing algorithms. *Exp. Fluids* 6: 373–80

Adrian, R. J. 1983. Laser velocimetry. In *Fluid Mechanics Measurements*, ed. R. Goldstein, pp. 155–244. Washington, DC: Hemisphere. 630 pp.

Adrian, R. J. 1984. Scattering particle characteristics and their effect on pulsed laser measurements of fluid flow: speckle velocimetry vs. particle image velocimetry. *Appl. Opt.* 23: 1690–91

Adrian, R. J. 1986a. Multi-point optical measurements of simultaneous vectors in unsteady flow—a review. *Int. J. Heat Fluid Flow* 7: 127–45

Adrian, R. J. 1986b. Image shifting technique to resolve directional ambiguity in double-pulsed velocimetry. *Appl. Opt.* 25(21): 3855–58

Adrian, R. J. 1988. Statistical properties of particle image velocimetry measurements in turbulent flow. In *Laser Anemometry in Fluid Mechanics—III*, ed. R. Adrian, T. Asanuma, D. Durão, F. Durst, J. Whitelaw, pp. 115–29. Lisbon: Ladoan-Inst. Super. Tec. 541 pp.

Adrian, R. J., Yao, C.-S. 1984. Development of pulsed laser velocimetry (PLV) for measurement of turbulent flow. In *Proc. Symp. Turbul.*, ed. X. Reed, G. Patterson, J. Zakin, pp. 170–86. Rolla: Univ. Mo. 380 pp.

Adrian, R. J., Yao, C.-S. 1985. Pulsed laser technique application to liquid and gaseous flows and the scattering power of seed materials. *Appl. Opt.* 24: 44–52

Adrian, R. J., Yao, C.-S. 1987. Power spectra of fluid velocities measured by laser Doppler velocimetry. *Exp. Fluids* 5: 17–28

Agui, J. C., Jiménez, J. 1987. On the performance of particle tracking. *J. Fluid Mech.* 185: 447–68

Akbari, H., Bjelkhagen, H. I. 1986. Holography in 15-foot bubble chamber at Fermilab. *Proc. Soc. Photo-Opt. Instrum. Eng.* 615: 7–12

Archbold, E., Ennos, A. E. 1972. Displacement measurements from double exposure laser photographs. *Opt. Acta* 19: 253–71

Arnold, W., Hinsch, K. 1988. Purely optical parallel processing in particle image velocimetry and the study of flow structures. *Proc. Conf. Opt. Methods in Flow and Part. Diagnostics, ICALEO '88*. Orlando, Fla: Laser Inst. Am. (Abstr.)

Arroyo, M. P., Yonte, T., Quintanilla, M., Savirón, J. M. 1988. See Chiang & Reid 1988, pp. 295–316

Barker, D. B., Fourney, M. E. 1977. Measuring fluid velocities with speckle patterns. *Opt. Lett.* 1: 135–37

Binnington, R. J., Troup, G. J., Boger, D. V. 1983. A low cost laser-speckle photographic technique for velocity measure-

ment in slow flows. *J. Non-Newtonian Fluid Mech.* 12: 255–67

Braun, M. J., Canacci, V. A., Russell, L., Hendricks, R. C. 1989. A laser based computer aided non-intrusive technique for full field flow characterization in macroscopic curved channels. In *Flow Visualization,* ed. M. Braun et al, FED-85: 15–22. New York: ASME. 149 pp.

Burch, J. M., Tokarski, J. M. J. 1968. Production of multiple beam fringes from photographic scatters. *Opt. Acta* 15: 101–11

Cenedese, A., Paglialunga, A. 1989. A new technique for the determination of the third velocity component with PIV. *Exp. Fluids* 8: 228–30

Chang, T. P., Wilcox, N. A., Tatterson, G. B. 1984. Application of image processing to the analysis of three-dimensional flow fields. *Opt. Eng.* 23(3): 283–87

Chiang, F. P., Reid, G. T., eds. 1988. *Optics and Lasers in Engineering* 9: 161–325. New York: Elsevier

Collicott, S., Hesselink, L. 1986. Anamorphic optical processing of multiple-exposure speckle photographs. *Opt. Lett.* 11: 410–12

Collicott, S., Hesselink, L. 1987. Real time speckle velocimetry with recording in photorefractive crystals. *AIAA Pap. No. 87-1376*

Coupland, J. M., Halliwell, N. A. 1988. Particle image velocimetry: rapid transparency analysis using optical correlation. *Appl. Opt.* 27: 1919–21

Dainty, J. C., ed. 1975. *Laser Speckle and Related Phenomena.* Berlin: Springer-Verlag. 342 pp.

Dimotakis, P. E., Debussy, F. D., Koochesfahani, M. M. 1981. Particle streak velocity field measurements in a two-dimensional mixing layer. *Phys. Fluids* 24: 995–99

Drain, L. E. 1972. Coherent and non-coherent methods in Doppler optical heat velocity measurement. *J. Phys. D* 5: 481–95

Dudderar, T. D., Simpkins, P. G. 1977. Laser speckle photography in a fluid medium. *Nature* 270: 45–47

Dudderar, T. D., Meynart, R., Simpkins, P. G. 1988. Full-field laser metrology for fluid velocity measurement. See Chiang & Reid 1988, pp. 163–200

Erf, R. K. 1980. Application of laser speckle to measurement. *Laser Appl.* 4: 1–69

Fage, A., Townend, H. C. H. 1932. Turbulent motion near a wall. *Proc. R. Soc. London Ser. A* 135: 656–77

Farrell, P. V., Goetsch, D. 1989. Optical analysis of particle image velocimetry data. In *ICALEO '89,* 68: 82–91. Orlando, Fla: Laser Inst. Am. 195 pp.

Frieden, B. R., Zoltani, C. K. 1989. Fast tracking algorithm for multiframe particle image velocimetry data. *Appl. Opt.* 28: 652–55

Gad-el-Hak, M., ed. 1989. *Advances in Fluid Mechanics Measurements.* New York: Springer-Verlag. 606 pp.

Gärtner, U., Wernekinck, U., Merzkirch, W. 1986. Velocity measurements in the field of an internal gravity wave by means of speckle photography. *Exp. Fluids* 4: 283–87

Gharib, M., Hernan, M. A., Yavrouian, A. H., Sarohia, V. 1985. Flow velocity measurement by image processing of optically activated tracers. *AIAA Pap. No. 85-0172*

Gheen, G., Cheng, L.-J. 1988. Optical correlators with fast updating speed using photorefractive semiconductor materials. *Appl. Opt.* 27: 2756–61

Goebel, S. G., Dutton, J. C. 1990. Velocity measurements of compressible, turbulent mixing layers. *AIAA J.* In press

Goodman, J. W. 1968. *Introduction to Fourier Optics.* New York: McGraw-Hill. 287 pp.

Grousson, R., Mallick, S. 1977. Study of flow pattern in a fluid by scattered laser light. *Appl. Opt.* 16: 2334–36

Guezennec, Y. G., Kiritsis, N. 1989. Statistical investigation of errors in particle image velocimetry. In *ICALEO '89,* 68: 130–40. Orlando, Fla: Laser Inst. Am. 195 pp.

Hassa, C., Paul, P. H., Hanson, R. K. 1987. Laser-induced fluorescence modulation techniques for velocity measurements in gas flows. *Exp. Fluids* 5: 240–46

Haussmann, G., Lauterborn, W. 1980. Determination of size and position of fast moving gas bubbles in liquids by digital 3-D image processing of hologram reconstructions. *Appl. Opt.* 19: 3529–35

Hesselink, L. 1988. Digital image processing in flow visualization. *Annu. Rev. Fluid Mech.* 20: 421–85

Höcker, R., Kompenhans, J. 1989. Some technical improvements of particle image velocimetry with regard to its application in wind tunnels. *Proc. Int. Congr. Instrum. in Aerodyn. Simul. Facil., Göttingen,* pp. 545–54

Huntley, J. M. 1986a. An image processing system for the analysis of speckle photographs. *J. Phys. E* 19: 43–48

Huntley, J. M. 1986b. Speckle photography fringe analysis by the Walsh transform. *Appl. Opt.* 25: 382–86

Huntley, J. M. 1989. Speckle photography fringe analysis: assessment of current algorithms. *Appl. Opt.* 28(20): 4316–22

Ineichen, B., Eglin, P., Dandliker, R. 1980.

Hybrid optical and electronic image processing for strain measurements by speckle photography. *Appl. Opt.* 19: 2191–95

Kaufman, G. H., Ennos, A. E., Gale, B., Pugh, D. J. 1980. An electro-optical readout system for analysis of speckle photographs. *J. Phys. E* 13: 579–84

Kawahashi, M., Hosoi, K. 1989. Beam-sweep laser speckle velocimetry. *Exp. Fluids* 8: 109–10

Keane, R., Adrian, R. J. 1990. Optimization of particle image velocimeters. Part I: double pulsed systems. *Meas. Sci. Technol.* In press

Kent, J. C., Eaton, A. R. 1982. Stereo photography of neutral density He-filled bubbles for 3-D fluid motion studies in an engine cylinder. *Appl. Opt.* 21(5): 904–12

Kerker, M. 1969. *The Scattering of Light and Other Electromagnetic Radiation.* New York: Academic. 666 pp.

Khalighi, B. 1989. Study of the intake swirl process in an engine using flow visualization and particle tracking velocimetry. In *Flow Visualization*, ed. B. Khalighi, M. Braun, C. Freitas, FED-85: 37–47. New York: ASME. 149 pp.

Kobayashi, T., Yoshitake, Y. 1985. An automated analysis method for determining velocity vector from a pathline photograph. In *Fluid Control and Measurement (Flucome Tokyo '85)*, ed. M. Hiada, pp. 729–34. New York: Pergamon. 1093 pp.

Kobayashi, T., Yoshitake, Y., Saga, T., Segawa, S. 1985. An image processing technique for determining two-dimensional flow fields with reverse flow. In *Physical and Numerical Flow Visualization*, FED-22: 39–46. New York: ASME. 130 pp.

Kompenhans, J., Höcker, R. 1988. Applications of particle image velocimetry to high speed flows. In *Particle Image Displacement Velocimetry*, ed. M. Riethmuller, pp. 67–84. Rhode-Saint-Genese, Belg: von Kármán Inst. Fluid Dyn.

Kompenhans, J., Reichmuth, J., Höcker, R. 1989. Data evaluation in particle image velocimetry by means of a spatial light modulator. In *ICALEO '89*, 68: 121–29. Orlando, Fla: Laser Inst. Am. 195. pp.

Landreth, C. C., Adrian, R. J. 1988. Electro-optical image shifting for particle image velocimetry. *Appl. Opt.* 27(20): 4216–20

Landreth, C. C., Adrian, R. J. 1989. Measurement and refinement of velocity data using high image density analysis in particle image velocimetry. In *Applications of Laser Anemometry to Fluid Mechanics*, ed. R. Adrian, T. Asanuma, D. Durão, F. Durst, J. Whitelaw, pp. 484–97. Berlin: Springer-Verlag. 535 pp.

Landreth, C. C., Adrian, R. J. 1990. Impingement of a low Reynolds number turbulent circular jet onto a flat plate at normal incidence. *Exp Fluids* 9: 74–84

Landreth, C. C., Adrian, R. J., Yao, C.-S. 1988. Double pulsed particle image velocimeter with directional resolution for complex flows. *Exp. Fluids* 6: 119–28

Lauterborn, W., Vogel, A. 1984. Modern optical techniques in fluid mechanics. *Annu. Rev. Fluid Mech.* 16: 223–44

Lee, S. J., Chung, M. K., Mun, C. W., Cho, Z. H. 1987. Experimental study of thermally stratified unsteady flow by NMR-CT. *Exp. Fluids* 5: 240–46

Lee, M. M., Hanratty, T. J., Adrian, R. J. 1989. An axial viewing photographic technique to study turbulence characteristics of particles. *J. Multiphase Flow* 15: 787–802

Liu, Z., Landreth, C. C., Adrian, R. J., Hanratty, T. J. 1990. Measurements in turbulent channel flow by high resolution particle image velocimetry. *Exp. Fluids.* In press

Lourenco, L., Krothapalli, A. 1987. The role of photographic parameters in laser speckle or particle image displacement velocimetry. *Exp. Fluids* 5: 29–32

Lourenco, L. M., Krothapalli, A. 1988. Application of PIDV to the study of the temporal evolution of the flow past a circular cylinder. In *Laser Anemometry in Fluid Mechanics—III*, ed. R. Adrian, T. Asanuma, D. Durão, F. Durst, J. Whitelaw, pp. 161–78. Lisbon: Ladoan-Inst. Super. Tec. 541 pp.

Lourenco, L. M., Whiffen, M. C. 1986. Laser speckle methods in fluid dynamics applications. In *Laser Anemometry in Fluid Mechanics—II*, ed. R. Adrian, D. Durão, F. Durst, H. Mishina, J. Whitelaw, pp. 51–68. Lisbon: Ladoan-Inst. Super. Tec. 518 pp.

Malyak, P. H., Thompson, B. J. 1984. Particle displacement and velocity measurement using holography. *Opt. Eng.* 23(5): 567–76

Merzkirch, W. 1987. *Flow Visualization.* New York: Academic. 260 pp.

Meynart, R. 1980. Equal velocity fringes in a Rayleigh-Bénard flow by a speckle method. *Appl. Opt.* 19: 1385–86

Meynart, R. 1983a. Instantaneous velocity field measurements in unsteady gas flow by speckle velocimetry. *Appl. Opt.* 22: 535–40

Meynart, R. 1983b. Speckle velocimetry study of vortex pairing in a low Re unexcited jet. *Phys. Fluids* 26: 2074–79

Meynart, R. 1983c. Speckle velocimetry: an application of image analysis techniques to the measurement of instantaneous ve-

locity fields in unsteady flow. In *ICIASF '83 Record*, pp. 30–36. New York: IEEE

Meynart, R. 1985. Non-Gaussian statistics of speckle noise of Young's fringes in speckle velocimetry. *Appl. Opt.* 24: 1448–53

Meynart, R., Simpkins, P. G., Dudderar, T. D. 1987. Speckle measurements of convection in a liquid cooled from above. *J. Fluid Mech.* 182: 235–54

Miles, R. B., Connors, J. J., Markovitz, E. C., Howard, P. J., Roth, G. J. 1989. Instantaneous profiles and turbulence statistics of supersonic free shear layers by Raman excitation plus laser-induced electronic fluorescence (Relief) velocity tagging of oxygen. *Exp. Fluids* 8: 17–24

Murai, S., Nakamura, H., Suzaki, Y. 1980. Analytical orientation for non-metric camera in the application to terrestrial photogrammetry. *Int. Arch. Photogramm.* 23: 516–25

Nishino, K., Kasagi, N., Hirata, M. 1989. Three-dimensional particle tracking velocimetry based on automated digital image processing. *J. Fluid Eng.* 111: 384–91

Paone, N., Riethmuller, M. L., Van den Braembussche, R. A. 1989. Experimental investigation of the flow in the vaneless diffuser of a centrifugal pump by particle image displacement velocimetry. *Exp. Fluids* 7: 371–78

Perkins, R. J., Hunt, J. C. R. 1989. Particle tracking in turbulent flows. In *Advances in Turbulence*, 2: 286–91. Berlin: Springer-Verlag

Pickering, C. J. D., Halliwell, N. A. 1984. Speckle photography in fluid flows: signal recovery with two-step processing. *Appl. Opt.* 23: 1128–29

Popovich, A. T., Hummel, R. L. 1967. A new method for non-disturbing turbulent flow measurements very close to a wall. *Chem. Eng. Sci.* 22: 21–25

Pratt, W. K. 1978. *Digital Image Processing.* New York: Wiley-Interscience. 750 pp.

Racca, R. G., Dewey, J. M. 1988. A method for automatic particle tracking in a three-dimensional flow field. *Exp. Fluids* 6: 25–32

Reuss, D. L., Adrian, R. J., Landreth, C. C., French, D. T., Fansler, T. D. 1989. Instantaneous planar measurements of velocity and large-scale vorticity and strain rate in an engine using particle-image velocimetry. *SAE Tech. Pap. No. 890616*, Soc. Automot. Eng., Detroit

Ricka, J. 1987. Photobleaching velocimetry. *Exp. Fluids* 5: 381–84

Robinson, D. W. 1983. Automatic fringe analysis with a computer image-processing system. *Appl. Opt.* 22: 2169–76

Simpkins, P. G., Dudderar, T. D. 1978. Laser speckle measurement of transient Bénard convection. *J. Fluid Mech.* 89: 665–71

Sinha, S. K. 1988. Improving the accuracy and resolution of particle image or laser speckle velocimetry. *Exp. Fluids* 6: 67–68

Stetson, K. A. 1975. A review of speckle photography and interferometry. *Opt. Eng.* 14: 482–89

Uemura, T., Yamamoto, F., Ohmi, K. 1989. A high speed algorithm of image analysis for real time measurement of two-dimensional velocity distribution. In *Flow Visualization*, ed. B. Khalighi, M. Braun, C. Freitas, FED-85: 129–34. New York: ASME. 149 pp.

Utami, T., Ueno, T. 1984. Visualization and picture processing of turbulent flow. *Exp. Fluids* 2: 25–32

Utami, T., Ueno, T. 1987. Experimental study on the coherent structure of turbulent open-channel flow using visualization and picture processing. *J. Fluid Mech.* 174: 399–440

Van Dyke, M. 1982. *An Album of Fluid Motion.* Stanford, Calif: Parabolic. 176 pp.

Vogel, A., Lauterborn, W. 1988. Time resolved particle image velocimetry. See Chiang & Reid 1988, pp. 277–94

Weinstein, L. M., Beeler, G. B., Lindemann, M. 1985. High-speed holocinematographic velocimeter for studying turbulent flow control physics. *AIAA Pap. No. 85-0526*

Willis, G. E., Deardorff, J. W. 1974. A laboratory model for the development of the unstable planetary boundary layer. *J. Atmos. Sci.* 31: 1297–1307

Zarschizky, H., Lauterborn, W. 1983. Digital picture processing on high speed holograms. In *ICIASF '83 Record*, pp. 49–56. New York: IEEE